Ultrafast Dynamics of Nanoparticles in Highly Intense X-Ray Pulses

vorgelegt von

M. Sc.
Maximilian Jakob Bucher

geb. in Frankfurt am Main

von der Fakultät II - Mathematik und Naturwissenschaften
der Technischen Universität Berlin
zur Erlangung des akademischen Grades

Doktor der Naturwissenschaften
- Dr. rer. nat. -

genehmigte Dissertation

Promotionsausschuss:

Vorsitzender:	Prof. Dr. Mario Dähne
Berichter/Gutachter:	Prof. Dr. Thomas Möller
Berichter/Gutachter:	Prof. Dr. Christoph Bostedt

Tag der wissenschaftlichen Aussprache: 24. Dezember 2016

Berlin 2016

M.Sc. Maximilian Jakob Bucher
Argonne National Laboratory
Chemical Sciences and Engineering Division
Argonne, IL 60439, United States
E-Mail: `buchermj@anl.gov`
Web: `https://www.max-bucher.de`

SLAC National Accelerator Laboratory
Linac Coherent Light Source
Menlo Park, CA 94025, United States

Technische Universität Berlin
Institut für Optik und Atomare Physik
10623 Berlin, Germany

This work is licensed under a Creative Commons “Attribution 4.0 International” license.

More information can be found under
`https://creativecommons.org/licenses/by/4.0/deed.en`

Abstract

abstract text here

Kurzfassung

deutsche Kurzfassung hier

Contents

1 Introduction 1

2 Fundamental Concepts 5

2.1 X-ray free electron laser 5
  2.1.1 Self amplification by spontaneous emission 7
  2.1.2 Soft X-ray self seeding 10
  2.1.3 Novel X-ray pump–probe techniques 13
2.2 Rare gas clusters 17
  2.2.1 Creation of a homogenous cluster 18
  2.2.2 Creation of a heterogeneous cluster 23
2.3 Introduction into X-ray scattering 25
  2.3.1 Small angle X-ray scattering 26
  2.3.2 The inverse problem: Phase retrieval 29
2.4 Light-matter interaction 31
  2.4.1 Ionization of matter 31
  2.4.2 Charge migration 35
2.5 Ionization of clusters in intense X-ray pulses 38
  2.5.1 Formation and expansion of a nanoplasma 38
  2.5.2 Imaging of transient states 40
  2.5.3 Tampered layers to inhibit the nanoplasma expansion 44

3 Experimental Setup 47

3.1 The atomic, molecular and optcal physics instrument at LCLS 47
3.2 The LAMP end-station at AMO 47
3.3 The large area pn-CCD detectors 47
3.4 Time of flight mass-spectrometer 47
3.5 Sample delivery 47

4 Methods **49**
4.1 The computing environment at LCLS 49
4.1.1 PSANA - Python interaction with LCLS computing 49
4.2 pnCCD photon detectors 49
4.2.1 Signal analysis 49
4.3 Combining multiple pnCCD detectors 49
4.4 Hitfinding 50
4.5 Phase retrieval from a single diffraction pattern 50
4.5.1 Solving the inverse problem 50
4.5.2 2D reconstructions and limitations 50
4.5.3 1D reconstructions 50
4.6 Summary of methods 50

5 Results and discussion **51**
5.1 Static data 51
5.2 Pristine xenon pump–probe data 51
5.2.1 iToF traces with xenon as sample 51
5.2.2 Xenon diffraction images 51
5.2.3 Reconstructions of xenon cluster single shot images 51
5.2.4 pnCCD image pump – probe considerations 51
5.2.5 Time of flight data 51
5.3 Pristine helium cluster pump-probe data 51
5.3.1 iToF data with helium as sample 52
5.3.2 Diffraction images of helium cluster 52
5.4 Helium-xenon core-shell systems and pump–probe data 52
5.4.1 Time-of-flight data of helium-xenon core-shell systems 52
5.4.2 Diffraction images of helium-xenon core shell systems 53
5.4.3 Core-shell system considerations 53
5.5 Conclusion of the X-ray pump – X-ray probe study 53

6 Summary and outlook **55**
6.1 Summary 55
6.2 Outlook 55

7 Appendix **A**
7.1 Python code on spherical integrations . . . . A
7.2 Python code on combining detectors . . . . A

8 Bibliography **C**

9 Index **O**

10 Acknowledgment **Q**

List of Figures

2.1 Aerial view of the Linac Coherent Light Source. 6

2.2 Schematic setup of an undulator. 7

2.3 Undulator gain curve correlated to microbunching. 9

2.4 Spectra of FEL SASE operation. 11

2.5 Spectra for Soft X-ray self-seeding and spectral brightness of various light-sources. 12

2.6 Schematic setup of undulator based pump–probe scheme. 15

2.7 Schematic setup of the bunch based pump-probe setup. 17

2.8 Schematic of a supersonic gas expansion into the vacuum. 19

2.9 Schematic of a pickup (gas-)source. 24

2.10 Principle of scattering rays of an atom. 28

2.11 Principle of a phase retrieval algorithm. 30

2.12 Total absorption cross-sections for helium and xenon. 32

2.13 Schematic illustration of common charge transfer processes 36

2.14 Fluoresence spectra from xenon and Auger spectra from neon. 37

2.15 Schematic illustration of the nanoplasma creation and expansion. 39

2.16 Measurement and simulation of the nanoplasma expansion in xenon cluster. 41

2.17 X-ray pump – X-ray probe scattering experiment on Xe-cluster that shows an early evolution of the nanoplasma transition. 43

2.18 Time of flight data of argon and xenon core-shell systems. 45

5.1 caption. MAKE IMAGE NICER 52

List of Tables

2.1 Parameter K values for rare gases [1]. 22
2.2 Differential absorption cross-sections and ionization potentials for xenon. . 34
2.3 Differential absorption cross-sections and ionization potentials for xenon and helium 34
2.4 Elastic scattering factors for helium and xenon. 35

1 Introduction

Investigating matter with light is one of the most fundamental approaches to study nature. Whether we look at things by eye or use more advanced methods for example using lasers, it is an invaluable tool to understand nature. Through light, we can study the shapes of objects, investigate fundamental particles, study quantum mechanics and so much more. Key aspect in almost any study involving light is it's wavelength. The wavelength of light can make you feel cozy at home with a modern LED light bulb or shroud your home in a blue, uncomfortable haze when you use older light bulbs. At the end of the 19th century, Röntgen discovered the then novel X-radiation and quickly realized its impact due to its different wavelength. Soon, he was able to take first medical X-ray images, later X-rays could be used to investigate fundamental aspects of atoms. The success story continues until today, where short wavelength X-rays enables the study of the workhorse in human bodies, namely proteins. The shape of a protein, which is only a few nanometers in size, cannot be seen in a microscope anymore and only X-rays can be used to unravel their shape with sufficient resolution. The shape of a biomolecules is of particular interest because it defines its biological function. The chemical structure of most human biomolecules are fairly similar and affect the function little. Medical drugs often aim to affect biological functions such that the specific shape of a protein becomes very important for drug research and drug design.

However, there is more to light than just its wavelength. The intensity of light plays a crucial role, for example when we are sitting in front of a fire and the warm glaze of infrared (IR) radiation can be felt on our skin. Anyway, using high intense radiation allows us to create an environment comparable to the inside of the sun, where fusion processes create energy and other interesting high energy processes are happening. Intense light is also needed if you want to study the very small because the interaction between matter and light becomes very small on length scales of for example a protein. To study the shape of a protein a certain interaction is needed and since we do not want to change the protein, we have to adjust the intensity of light.

Last but not least, light can come in short flashes for example when taking a photograph. At night, when the flash is too long, the pictures often get washed out. It is similar when you study nature, if you want to look at some movement or more general dynamics, your light flash must be short enough to resolve this dynamic, otherwise it gets washed out. Proteins function also through movement. Many of their dynamics could already be deciphered but it is unclear what one would discover if one would look at even faster timescales.

Summarizing, a light flash can be described by by its wavelength, intensity and duration. To study matter, e.g. proteins, one has to optimize these three parameters a lot. TTherefore, a new kind of light source was developed that is particularly interesting for imaging the very small on the nanometer scale. The first one of these light sources, a so called free electron laser (FEL), was build in Hamburg, Germany. First experiments with FELs that showed proof of principle studies showcasing capabilities of FELs as a highly intense and ultra short light pulse source. As a result, more advanced X-ray free electron laser (XFEL) were built to further improve capabilities. The first hard XFEL was built in Menlo Park, California at Stanford University and is called the Linac Coherent Light Source (LCLS). It is a 4.1 km long machine[1], the most straightest building in the world[2], is build underneath the ground and the interstate I-280 crosses it via a bridge[3]. This massive machine delivers what is needed to use imaging techniques that have been out of reach so far. To name a few, with LCLS it is possible to study protein crystals of much smaller size, one can study single particles for example viruses and cells. And LCLS is not limited to imaging techniques, one can study atoms and molecules in thus far unreachable regimes and also understand magnetism better. The reason these new areas of study area accessible through LCLS lay in the light parameters. LCLS produces light with a very short wavelength (X-rays from 4.6 nm to 0.1 nm), it has a very high intensity ($10^18Ws/cm^2$) and ultra short pulses ($1-500fs$). The combination of these parameters is unique in the world and enables us to look at things that have been hidden so far.

Let us now imagine that we expose a protein to the very intense X-rays from LCLS (or any other XFEL). Within the first moment of interaction from the light and the proteins, the protein scatters photons distinctive to it shape that we are able measure and hence recover the shape of the protein. But the protein will also absorb the light and therefore energy and will become very hot, much like the conditions on the surface of the sun. The hot protein will expand quickly and disintegrate into its atomic components. While the scattering process is desired the inevitable absorption process will ultimately hinder the scattering process and limit the resolution of our measurement. The damage that occurs to the sample is an ultra-fast process that can only be studied with an even faster light pulse. It is a process that thus far is known to exist but has been hidden due to the limitation of other light sources. XFEL offer now the opportunity to study this process that is applicable to a variety of X-ray imaging techniques ranging from crystallography to spectroscopic applications over to the imaging of single particles.

---

[1] Measurement on Google maps from the injector building to the far experimental hall.

[2] The European XFEL in Hamburg, Germany is currently build to similar engineering requirements.

[3] On a fun note, the accelerator part of LCLS is actually older than the I-280 and do avoid interruptions of the experiments, the bridge was build long before the intersate and there are pictures of this bridge that is not connected to any streets.

This thesis discusses an experiment performed with LCLS to study the effects and dynamics induced by radiation damage on homogenous xenon and helium clusters and heterogeneous clusters consistent of xenon and helium. A detailed and time-resolved X-ray pump – X-ray probe study is undertaken to first induce X-ray related dynamics via a X-ray pump pulse and then create a single-shot image of the cluster at a given time delay. We combine the single particle imaging technique with a time-of-flight mass spectrometer that yields insights into ionization dynamics, absorbed energies and particle heterogeneity. Rare gas clusters are used as sample target as they are an ideal nanosamples in the gas phase. They are easy to produce and easy to transport to the interaction region with LCLS. Furthermore they can be tuned in size and multiple rare gases, here xenon and helium, can be combined to form a single nanometer sized heterogeneous cluster. We present the data from the study in form of real space images from clusters complemented by diffraction images. Furthermore, we correlate the time-of-flight data to each image.

The thesis is organized as follows, chapter 2 discusses fundamental aspects and background information to the performed studies. Chapter 3 focuses on the experimental setup of this study, chapter 5 presents the results obtained and finally 6 sumarises the previous chapters and provides an outlook for further studies.

2 Fundamental Concepts

This chapter tries to condense some of the theoretic basics that will reoccur throughout the thesis. We start off with an introduction to the key aspects of X-ray free electron lasers including the more specific parts of self-seeding and X-ray pump – X-ray probe techniques in section 2.1. This is followed by a section about the formation of rare gas clusters and a particular emphasis on supersonic jets and pickup sources in section 2.2. We then dive into the interaction of light and matter, starting with X-ray scattering including the broad topic of phase retrieval in diffraction patterns in section 2.3 and ending with the ionization of matter and formation of a nanoplasma.

2.1 X-ray free electron laser

The advance of X-ray free electron laser in the recent years has enabled experimental ideas from long ago but has also opened entirely new branches to research [2, 3]. So, let us start by investigating how that is. Thus far mostly synchrotron radiation facilities have provided X-rays to a great variety of scientific communities. In a synchrotron facility, a number of electron bunches is accelerated near the speed of light and then injected into a storage ring. Here, the electrons create an X-ray beam. The characteristics of this beam is called spectral brightness [4] or sometimes brilliance. We can define the spectral brightness as [5]

$$B = \frac{n}{A\ \Theta\ t\ \Delta E}, \tag{2.1}$$

with n being the number of photons, A the unit source size, Θ the divergence of the beam, t the pulse duration and ΔE the spectral bandwidth of the light pulse. The spectral brightness is an overall measure of the quality of a light source. The development of modern synchrotron light sources is hence often measured and compared to previous achieved values. The motivation in the improvement of the spectral brightness is to let a sample interact with as many photons possible, in the shortest time as possible, with an energy resolution as best as possible. In other words, more brilliant light sources are needed to create images of even smaller particles, or look at dynamics that are even faster. To increase the spectral brightness drastically in the X-ray regime, one intended

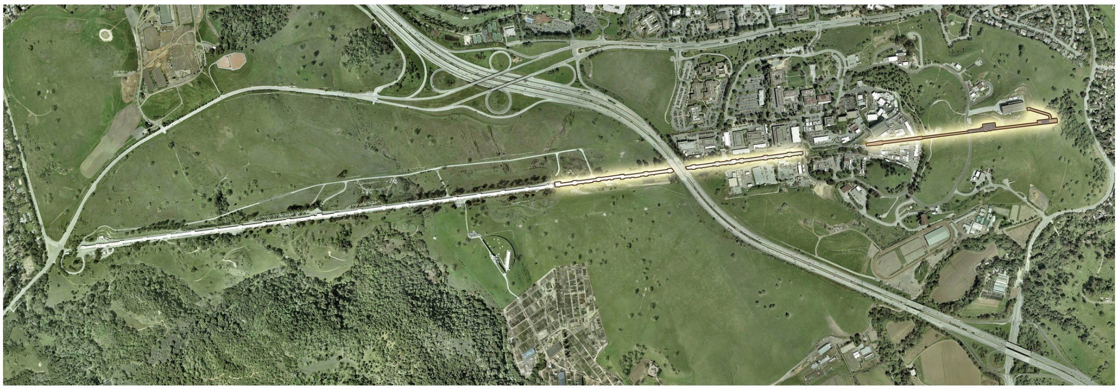

Figure 2.1: Aerial view of the Linac Coherent Light Source (LCLS). LCLS uses the last third of the SLAC Linear Accelerator but is overall a 4.1km long machine. The accelerator and buildings are stretched far because of the process light is generated. From [6]

to build a laser alike X-ray source. To give a numerical example and to get a better understanding of the improvements needed, let us look at absorption dynamics in atoms and molecules. One can conservatively estimate that a typical cross section at soft X-rays (1 nm wavelength) is around $\sigma = 1$ megabarn (Mb) [7]. Typical X-ray focii are round $A = 1\mu\text{m}^2$[1] such that the number of photons needed n_{in} to absorb just 1 photon per atom n_{abs} can be calculated by

$$n_{in} = \frac{n_{abs}A}{\sigma} = \frac{10^{-8}\text{cm}^2}{10^{-18}\text{cm}^2} = 10^{10} \qquad \text{photons} \tag{2.2}$$

An example of a modern synchrotron source is NSLS-II and a rough estimate yields that it produces roughly 1.710^4 photons per pulse in the Si111 bandwidth at pulse durations of a few ten picoseconds [8]. That is far out of reach to investigate non-linear, or multi-photon, processes. While this back on the envelope type of calculation might be off by an order of magnitude or so depending on the specific case, it illustrates the order of magnitude improvement scientists were looking for. Unfortunately, synchrotron sources are not able to produce these conditions currently and regular optical laser methods can not easily be extended to also create X-rays. A United States defense program in the 80's wanted to use an X-ray beam as anti-(space)missile defense, where the X-ray beam was apparently generated through ignition of an atomic bomb [9]. So, to reach the drastic higher number of photons per light pulse needed, it was proposed to build free electron laser [10, 11]. Free electron laser, amplify the light along a straight line to create

---

[1] Focus size at the AMO endstation at LCLS.

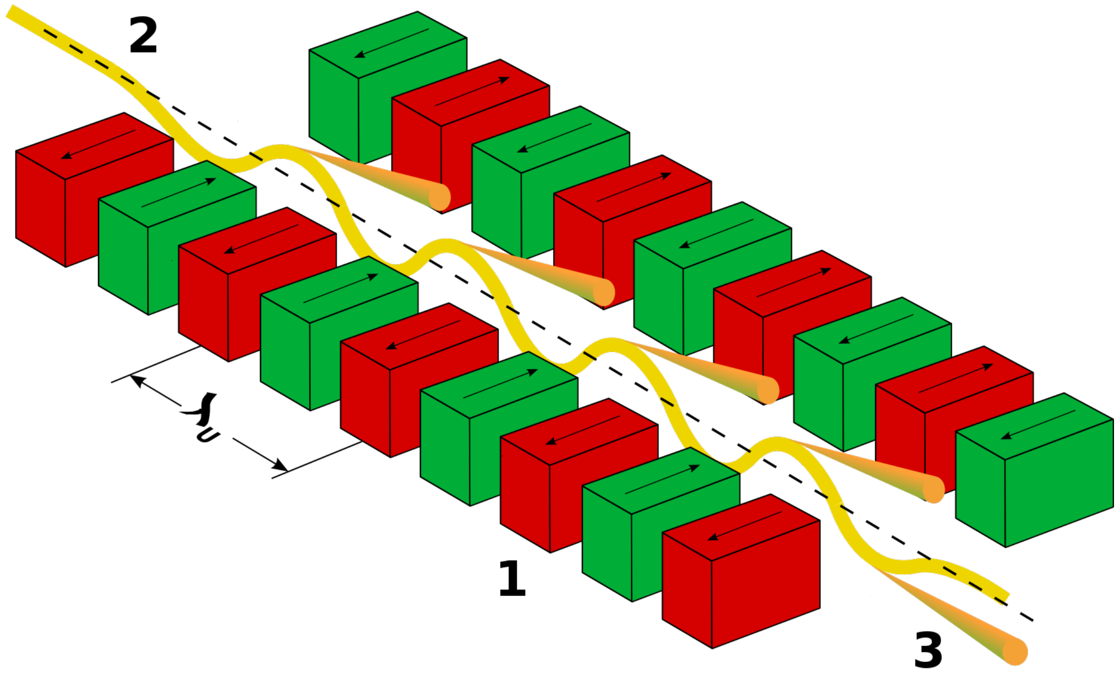

Figure 2.2: Schematic setup of an undulator with a period of λ_U. (1) Magnets in alternating polarity; the arrows indicate the direction of the magnetic field. (2) Incoming electron bunch near the speed of light. (3) Emitted light in beam direction due to sinusodial movement of the electron bunch. [12]

laser alike radiation[2]. In the birds eye view of the Linac Coherent Light Source in figure 2.1, one can imagine that it took several decades to build these kinds of sources. Today, free-electron lasers are able to increase the number of photons per pulse to currently $n_{in} = 10^{12}$ and achieve pulse lengths of a few femtoseconds. These are remarkable beam parameters and as a result LCLS was increasing the spectral brightness by many orders of magnitudes[3].

2.1.1 Self amplification by spontaneous emission

In synchrotron lightsources as well as free electron lasers, X-rays are generated using wiggler and undulator magnets. In principle, an electron bunch is accelerated near the speed of light and then wiggled along its path using magnetic fields. The wiggling causes the particles to emit radiation. Wigglers consist of magnets that are arranged in an alternating order to force the electron bunch on a sinusoidal trajectory. In a Wiggler, the electrons emit a total power $P_{emitted}$ that is proportional to the number of magnets m [13]

---

[2] The process to of the light create is explained in details in section 2.1.1.

[3] See figure 2.5 for an illustration of the improvement in brilliance.

$$P_{emitted} \propto m, \quad \text{in a wiggler magnet.} \tag{2.3}$$

The emitted radiation has a broad, continuous spectrum and the center of that spectrum can be controlled by changing the speed or kinetic energy of the electron bunch. Wigglers have been used at the Stanford Synchrotron Radiation Lightsource (SSRL) in 1979 to generate X-rays and were a great success. Continued development on the Wiggler design led to the idea of undulators. A schematic setup of an undulator magnet can be seen in figure 2.2. Wigglers and undulators create radiation because of the same principle, an electron bunch is accelerated near the speed of light and then forced on a sinusoidal pathway. In undulators, the separation of such magnets or undulator period λ_U and magnetic fields are chosen such that the emitted radiation per period constructively interferes with each other. The emitted wavelengths of undulators have a much more narrow pattern than that of wigglers and because, strictly speaking, only one wavelength is amplified the emitted power P_W now scales with [14]

$$P_{\text{emitted}} \propto m^2, \quad \text{in an undulator magnet} \tag{2.4}$$

We can characterize an undulator by the undulator strength parameter K and it is given by [15]

$$K = \frac{e \, B_{\text{max}} \, \lambda_U}{2\pi \, m_e \, c} \tag{2.5}$$

with the constants e being the electron charge, B_{max} being the maximum magnetic field in the undulator, m_e being the mass of an electron and c being the speed of light, we can write in convenient units

$$K \approx 0.934 B_{max} \, \lambda_U \qquad [\text{T cm}]\,. \tag{2.6}$$

Undulator magnets are large constructs of a few meters and their undulator period is on the order of centimeter. The electrons emit radiation in the nanometer wavelength regime because the electrons near the speed of light have to be considered relativistic and in the view of the electrons the undulator period λ_U appears shorter. We can correct for the relativistic effects and express the main amplified wavelength λ_r by [15]

$$\lambda_r = \frac{\lambda_U}{2\gamma} \left(1 + \frac{K^2}{2} + \gamma^2 \Psi^2\right), \tag{2.7}$$

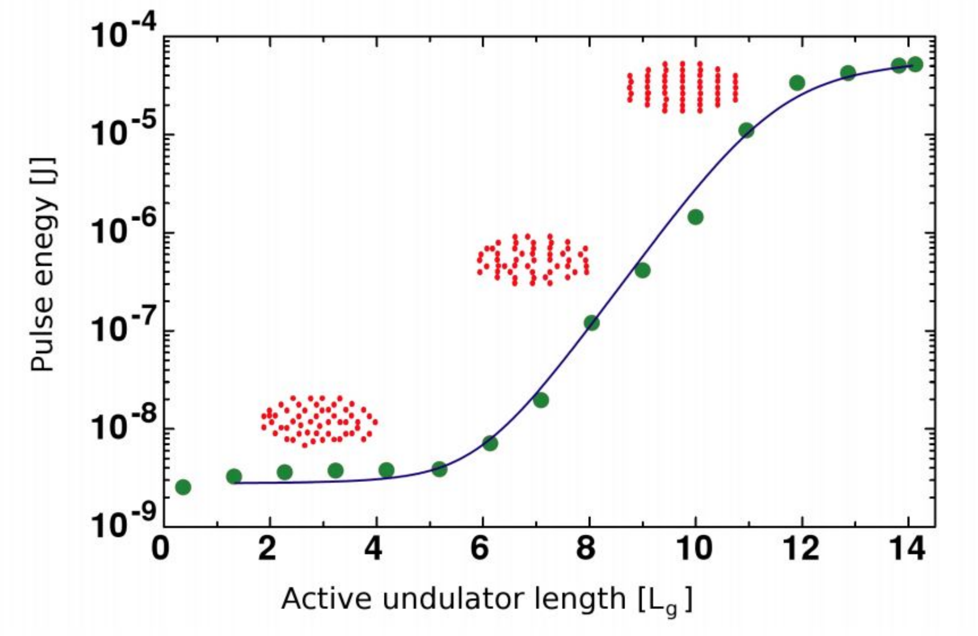

Figure 2.3: Undulator gain curve correlated to microbunching. The X-ray pulse energy is plotted algorithmically over the undulator length L_g (blue curve, green dots) and shows an exponential growth until saturation. The electron bunch (red dots) is starts with a random density distribution, as the bunch travels through the undulator modulates the electron density and the electrons are microbunched. Upon optimal microbunching, the X-ray lasing process saturates. From [16, 17]

with the kinetic energy γ of the electron beam in the undulator and Ψ its observation angle. Equation 2.6 and 2.7 also show that the wavelength in an undulator is determined by the undulator gap λ_U, the magnetic field B in the undulator and the kinetic energy of the electron beam γ.

Undulators are also used in X-ray free electron lasers. The main difference to synchrotron radiation sources is that the light is amplified over a much longer straight line using multiple undulator magnets serially connected. LCLS has a 112m long undulator section. Over the course of this distance, microscopic effects start to play a role that could be neglected in typical synchrotron radiation sources. In vacuum, light will always be faster than electrons near the speed of light. This slight difference means that the co-propagating photons and electrons have a phase difference and interact with each other. Depending on the phase, an electron will either gain or loose velocity. Over each undulator period, we can describe this *slip* with $\lambda_r(\Psi = 0)$. As a result, the initial unifrom electron density in the electron bunch is periodically modulated and the modulated electron bunch structure is called *microbunching.* The creation of micobunching as it travels through undulators is illustrated in figure 2.3. The increasingly structured electron beam amplifies a more narrow wavelength bandwidth and the number of electrons that are in phase with the photons increases over the travel length through the undulator. The electrons interact with the light field because of their narrow spatial and kinetic energy distributions. These parameters are characterized as the *emittance* of an electron bunch. Only the linear accelerator of a FEL are able to compress the electron bunch in space and energy, i.e. create a low emittance electron bunch, such that it can interact with the photons as described above. The initial process that starts this light amplification is triggered by the first few photons that are spontaneous emitted and then subsequently amplified. Hence, this type of radiation (or FEL operation mode) is called *Self Amplification by Spontaneous Emission* (SASE). It achieves laser alike amplification of the radiation power P_{SASE} that scales with the number of electrons N_e^2 [see 5, p. 61]

$$P_{SASE} \propto N_e^2, \quad \text{SASE operation} \tag{2.8}$$

The characteristics of SASE radiation are its noisy and spiky photon spectrum, as seen in figure 2.4, that come from the initial random (spontaneous) emission of photons.

X-ray free electron laser use one electron bunch and create one light pulse in a long set of undulator magnets, this is also called a *single-pass high-gain* FEL. Due to the lack of optics, X-ray FEL operate in the high-gain mode. A X-ray FEL gain curve as a function of gain length L_g can be seen in figure 2.3. The electron bunch travels over a long distance in the undulators until it eventually reaches saturation. In saturation, the microbunching is most developed. Since the creation of X-rays is affected by the kinetic energy of the electron bunch γ the electron bunch is not reused.

2.1.2 Soft X-ray self seeding

Free electron laser also have different operating modes than SASE. Particular interesting is the *seeded* type of operation, where the FEL amplifies an initial seed of photons. The photons seed can be created through various processes. Here again, the wavelength of the photon seed is the critical parameter in determining which method to choose. For example, in the infra red (IR) to extreme ultra violet (XUV) regime, conventional lasers can be used to place the initial photons seed. However, due to the lack of lasers available at soft and hard X-rays wavelength regimes, the idea of *self-seeding* gained traction. In

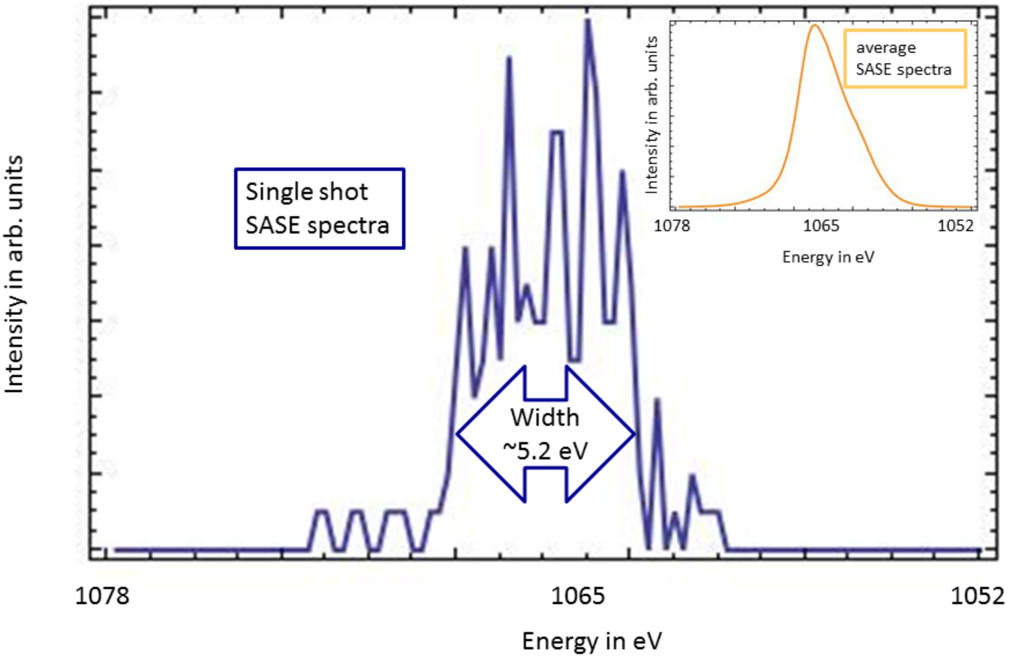

Figure 2.4: Spectra of FEL SASE operation. The large blue spectra is a SASE spectra from a single FEL shot using a photoelectron spectrometer as described in [18]. Note the spiky peak structure on a pedestal, within the narrow bandwidth of a FEL pulse some energies are getting more strongly amplified due to the microbunching. The yellow inset is an average spectra under the same conditions as the single-shot. Note the low energy tail in the spectra, which is due to FEL-jitter.

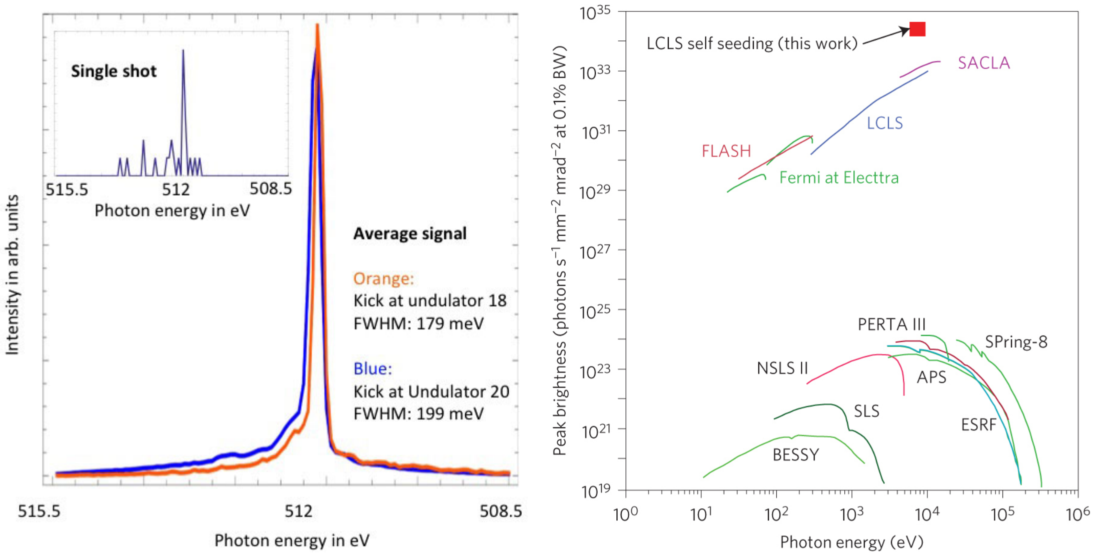

Figure 2.5: Left, normalized and average spectra of soft X-ray self seeding operations using the SXRSS and AMO instrument at LCLS [18]. The self-seeding spectra is characterized by a sharp spectral peak around a desired energy accompanied by a SASE radiation type spectral pedestal. If the electron bunch travel length is shortened, here kick at LCLS undulator 18 vs. 20, the undesired SASE pedestal is suppressed. The right image shows the peak spectral brightness of various light sources over a wide photon energy range. Soft X-ray self-seeding has a spectral brightness that exceeds current SASE FEL sources, however, the overall pulse energy is lower compared to SASE operations. From [19].

self-seeding, an electron bunch is first send through a few undulator magnets to generate a few SASE photons, the electrons and photons are then separated using a magnetic chicane, which also neutralizes the microbunching in the electron bunch. The monochromator selects a small wavelength slice from the comparably broad SASE spectrum of the initial photons. The photons exiting the monochromator are considered the *seed*. The seed and the electron bunch are overlapped again using the magnetic chicane and then send through more undulators. The seed generates now the microbuching, which is wavelength depended and thus a narrow wavelength band is amplified. Self-seeded beam operations have recently been demonstrated at LCLS. At hard X-rays, the Hard X-Ray Self-Seeding (HXRSS) instrument uses a diamond crystal to select a wavelength slice [20]. At soft X-rays, the Soft X-ray Self Seeding (SXRSS) instrument uses a grating as dispersive element [21]. A typical spectrum of a soft X-ray self-seeded beam can be seen in the left figure 2.5. The characteristics of this spectrum are an intense peak at the selected wavelength regime on top of a broad SASE background. The background is an artifact of the amplification of some spontaneous emission events and can be suppressed by using fewer undulator magnets. Self-seeded beams have a significantly reduced pulse energy by an order of magnitude or so, depending on the exact beam parameters, as compared to SASE operations. However, in their main peak, self-seeded beams have a higher spectral brightness when compared to a SASE spectrum. SASE spectra usually have a broad spectral bandwidth with a ΔE of a few eV, comparing seeded beams with equation 2.1 to SASE beams the increase in spectral brightness using seeded beams is understandable and is illustrated in the right figure 2.5. The peak intensity in a narrow spectral band makes seeded beams interesting for a variety of applications particular in condensed matter physics, where it is instrumental to excite with narrow bandwidth photons. Of course there are also applications in atomic and molecular physics, ranging from linear absorption spectroscopy [22], to ultrafast photoemission spectroscopy on molecules [18], to non-linear stimulated Raman spectroscopy [23], to ultra-fast photoemission studies. Particular interesting for this work is the magnetic chicane from the SXRSS instrument that has been used as described in the next chapter.

2.1.3 Novel X-ray pump–probe techniques

In order to study X-ray induced methods using X-ray imaging and spectroscopy techniques, as it is discussed in the present work, two X-ray pulses are needed . Here, a pump pulse is used to induce dynamics in the sample system and a probe pulse is used to probe them at a certain time delay Δt. Pump–probe experiments are commonly used as they allow a precise study of dynamics. The pump pulse gives a very controllable starting point, i.e. time zero in the dynamic process, and the probe pulse can perform a measurement at a later time delay Δt. Sometimes pump and probe pulse are switched, which is indicated by a negative time delay Δt, often to verify time zero or to probe the system before any dynamics have occurred.

Creating two X-ray flashes to create a pump–probe experiment is a technical challenge and again this challenge is due to the lack of optics and the availability and size of X-ray SASE sources. In order to overcome this challenge, two methods have been proposed. Method one, mirror based beam-split and delay systems [24, 25] that split one pulse into a pump and probe beam and allow the delay of the latter. These systems typically are limited to short delay times, as the optics have to fit into existing setups and have a low transmission of X-rays over the mirrors. Method two, uses accelerator based schemes [26, 27] that manipulate electron bunches to create two X-ray pulses. Limitations arise depending on the scheme, e.g. limited pulse delay Δt or pulse energy split through limited electron beam separation or length of magnetic chicane. Both methods have been demonstrated at LCLS and have found use to complement the more widely available optical laser pump– X-ray probe methods particularly in the chemical sciences [28–30].

As the accelerator based X-ray pump – X-ray probe method using a magnetic chicane has been used, let us describe these schemes in greater detail. Before we jump into the technical details, it is good to know that not only the aspect of creating a time delay Δt between the pump and the probe pulse is important but also to create a difference in wavelength between these two pulses. Generally, this is of use to resonantly pump and off-resonance probe or vice versa. Equation (2.7) indicates which parameters can be tuned to create two pulses of different color. One, the undulator parameter K can be tuned to change the emitted wavelength, or two, the lorentz factor γ can be different if there are two electron bunches. The undulator period λ_U is fixed at LCLS.

Undulator parameters $K_{1,2}$ based pump–probe scheme

The first developed accelerator based pump–probe technique at LCLS [26] uses a difference in undulator parameters $K_{1,2}$ to create two pulses of different wavelength, the time delay is introduced through a magnetic chicane and a schematic setup can be found in Figure 2.6.

In scheme I, one electron bunch is created through a single slotted foil[4] The use of the

---

[4] A single slotted foil or emittance-spoiling foil works comparable to a monochromator. It leaves a certain energy band of the electron bunch within the slot unspoiled and Coulomb scatters or spoils (compare to apertures) the rest. The 'dispersive' element is a magnetic chicane. By narrowing the electron beam one also reduces its pulse duration [31].

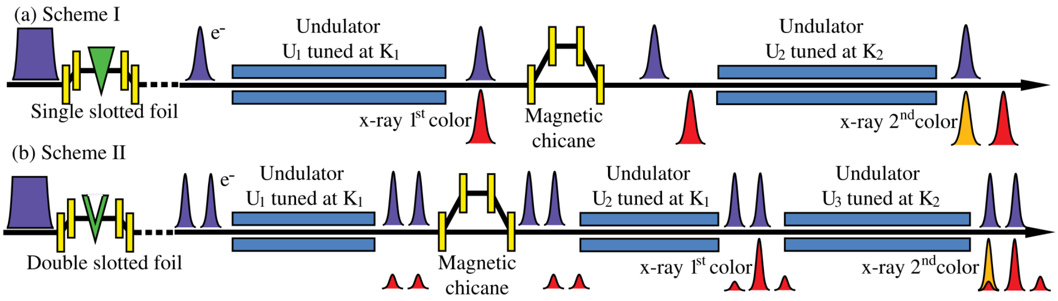
(a) Scheme I
e-
Undulator
U1 tuned at K1
Single slotted foil
x-ray 1st color
Magnetic
chicane
Undulator
U2 tuned at K2
x-ray 2nd color
(b) Scheme II
e-
Undulator
U1 tuned at K1
Double slotted foil
Magnetic
chicane
Undulator
U2 tuned at K1
x-ray 1st color
Undulator
U3 tuned at K2
x-ray 2nd color

Figure 2.6: Schematic setup at LCLS of undulator parameter K_i based pump–probe schemes. Scheme I creates one electron bunch using a single slotted foil and scheme II creates two electron bunches using a double slotted foil. The electron bunches emit radiation with a wavelength depending on K_i. A time delay Δt between pulses is introduced using a magnetic chicane. Figure from [26] reprinted with permission from APS.

slotted foil enables control over the pulse duration. The electron bunch then travels through an undulator section U_1 tuned at strength parameter K_1 and is stimulated to lase but the process does not go into saturation to be able to reuse the electron bunch in the second undulator section. The time delay Δt between the two pulses is introduced by a magnetic chicane. At LCLS, a dedicated chicane, e.g. from the soft X-ray self-seeding instrument, can reach up to

$$\Delta t_{max} = 800fs. \tag{2.9}$$

The minimal time delay can be achieved by setting the deflection in the magnetic chicane to zero in which case

$$\Delta t_{min} = \frac{l}{v_{el\ drift}} - \frac{l}{c} \approx 0fs, \tag{2.10}$$

with $l \approx 4m$ being the length between undulator sections U_1 and U_2 and c being the speed of light and $v_{el\ drift}$ being the drift velocity of the electron bunch. As the electron bunch travels close to the speed of light t_{min} is typically on the tens of attosecond timescale. The timing jitter between the two light pulses using only one electron bunch comes solely from the magnetic chicane due to the magnetic field jitter and the electron beam energy jitter. The total contribution to the timing jitter is less than 0.4% of the tim delay Δt imposed by the chicane. Since the delay chicane does not contribute significantly to the delay Δt a bigger factor is the velocity mismatch of the light pulse and the electron bunch. This mismatch can be estimated by

$$\Delta t_{beam\ mismatch} = \frac{N_u \lambda_r}{c}, \tag{2.11}$$

with N_u being the undulator periods. Given the parameters in study [26], $t_{beam\ mismatch} = 3fs$ such that a partial overlap could be achieved. However, the magnetic chicane removes the microbunching from section U_1. In undulator section U_2 tuned to undulator strength parameter K_2 the electron bunch lases again and the process is able to saturate. The maximal color separation between the two pulses is 1.9% in relative difference between K_1 and K_2.

Scheme II uses a double slotted foil[5] to create two electron beams. The two beams have a longitudinal separation that translates into the time delay Δt. The electron bunches travel through a first set of undulators U_1 that creates two pulses of the same wavelength, due to the shortness of the section U_1 the lasing process does not saturate. The electron bunches are then delayed using a magnetic chicane such that the leading electron bunch overlaps with the trailing light pulse. This light pulse now functions as a seed for the leading electron bunch such that this pulse saturates in undulator section U_2. The electron bunches then travel through the magnets at U_3, where the trailing electron bunch creates a second saturated pulse, the leading electron bunch barely emits radiation in U_3 since its energy spread has become too large after lasing in U_2. Using this method, two saturated lasing pulses can be generated, however, temporal overlap cannot be achieved.

Twin bunch or Lorentz factor γ based pump–probe scheme

The second developed accelerator-based pump-probe technique at LCLS [27] uses two electron bunches of different energy. A schematic setup of this beam operation can be found in figure 2.7.

The bunches are created through a double laser pulse that impinges on a photocathode. Initially, these two bunches have a time delay of a few picoseconds, however, two magnetic chicanes compress the electron bunches in the time and intensity domain such that a time delay on the ten femtosecond timescale is achieved. The electron bunches then travel through one undulator section and both pulses saturate in their lasing process. At $8.3k$ eV, both pulses combined can reach pulse energies of $1.2mJ$, the color separation is 100 eV and the time separation ranges from $\Delta t_{min} = 0fs$ to $\Delta t_{max} = 100fs$. At hard X-rays, this method requires the pump pulse to have a higher photon energy than the

---

[5] A double slotted foil works as a single slotted foil but it leaves to parts of the electron beam unspoiled through the two slots.

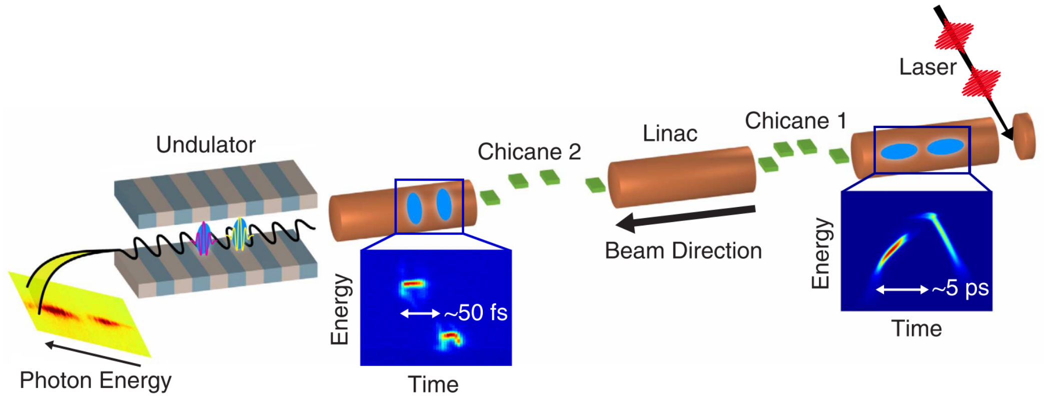

Figure 2.7: Schematic setup of the two bunch, two color pump–probe setup at LCLS. Two laser pulses shot at a cathode create two electron bunches with a delay Δt on the picosecond timescale. Two magnetic chicanes compress the bunches such that a delay Δt on the up to the ten femtosecond timescale is achieved. Both pulses go through one undulator section and the SASE lasing process is saturated. The relative color separation is on the order of 1%. From [27, 🅭🅯].

probe pulse, although their respective intensities may vary. However, this method is not restricted to hard X-rays and can be utilized at soft X-rays. In the soft X-rays wavelength regime, where the above explained slotted spoiler foil can be used. This allows a further control to tune the time delay of the electron bunches, which enables scanning across each other.

2.2 Rare gas clusters

Rare gase clusters have been used as nanosample in this study and this chapter will explore this topic. Clusters have a long history to study light-matter interaction as their characteristics are well known [32]. Generally speaking, clusters are an aggregation of atoms or molecules and vary in size. Their size can range from a few atoms to mesoscopic sizes such that one can classify a cluster as a bulk material. Clusters can form exotic materials that are interesting to study and can be well simulated through comparably simple computer models. Besides these testbed characteristics, the use of clusters has often practical purposes. They can be comparably easily generated and are typically easily tune able in size. Rare gas clusters are a subclass of clusters and they are bound by van der Waals forces and normally neutral-charged. Single van der

Waals cluster typically form in an icosahedral[6] shape when they are sufficiently small (up to nanometer sized) [33] and have mostly a fcc-crystal[7] structure but exhibit also hcp-crystal[8] structures [34, 35]. The creation of homogenous and heterogeneous rare gas clusters shall be the focus of the next few chapters.

2.2.1 Creation of a homogenous cluster

Rare gas clusters, for example xenon clusters, can be generated through a variety of ways. While there are many ways to explain the cluster formation process, a kinetic model [36] gives a very intuitive way in the microscopic processes. In this kinetic model, atoms and clusters grow through collisions. We can express these collisions mathematically through the following reaction formula

$$A_n + A \rightleftharpoons A^*_{n+1}, \quad n = 1, 2, ..., \quad \text{monomer collision,} \tag{2.12}$$

where a body A_n collides with a monomer A and form a metastable state A^*_{n+1} that will dissociate if not a subsequent collision deactivates it

$$A^*_{n+1} + M \rightleftharpoons A_{n+1} + M, \quad \text{activation/deactivation.} \tag{2.13}$$

M is a chaperone that can be any kind of third body that removes energy from the system. Note that a chaperone M can also activate the state again. The binding force behind rare-gas clusters is the Van der Waals force, hence they are called Van der Waals cluster sometimes.

While the early stage of the cluster growth is driven by the monomer addition, cluster-cluster coagulation start to dominate the later growth processes [37, 38]. This is due to the quantitative increase in small clusters in the generation process that then start to collide, similar to above kinetic model. From empirical evidence, we know that clusters solely generated through monomer addition have a size distribution of an exponential decay, whereas larger clusters that grew through coagulation follow a log-normal distribution. So through coagulation, the density of smaller clusters (and monomers and dimers) decreases through to cluster-cluster coagulation and larger clusters are formed. The most probable size of a cluster, i.e. the maximum of the log-normal distribution, is given by the parameters of the supersonic jet setup, which is what we will discuss next.

Supersonic jet setups typically store gas in a reservoir at a certain stagnation pressure

---

[6] An icosahedron is a polyhedron with 20 faces, i.e. a dice with 20 faces.

[7] fcc is short for face-centered cubic. A very common crystal structure.

[8] hcp stands for hexagonal close-packed and is also a crystal structure.

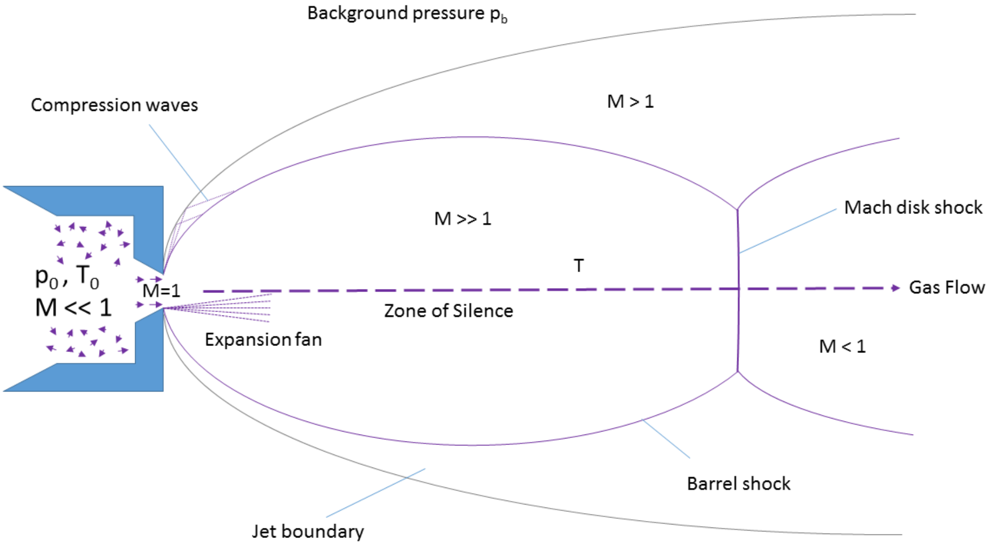
Background pressure p_b
Compression waves
M > 1
M >> 1
Mach disk shock
p_0, T_0
M << 1
M=1
T
Gas Flow
Zone of Silence
Expansion fan
M < 1
Barrel shock
Jet boundary

Figure 2.8: Schematic of a supersonic gas expansion into the vacuum. Gas is stored in a reservoir at pressure p_0, temperature t_0 and speed of the gas is thermal distributed ($M \ll 1$). As the gas enters the nozzle area, it is accelerated to the speed of sound ($M = 1$) and as the gas expands, the temperature T drops altering the speed of sound alters such that the gas now travels supersonic ($M \gg 1$). See text for details. After [39]

p_0 and temperature T_0. The gas expands through a nozzle into a vacuum and figure 2.8 shows a schematic drawing of this process. Typical values for p_0 are 10 bars, where the mean free path of the atoms is much smaller than the nozzle diameter D. This is why many collisions occur during the expansion in the nozzle and the above described kinetic theory explains the cluster formation. However, this holds not true in the supersonic molecular flow region, where no further cluster growth happens. To understand the expansion process in detail, we assume to work with an ideal gas and to describe the gas expansion itself, we further assume that no clusters are formed and that turbulence and effects of heat conduction are unimportant [32, 40].

To begin, the velocity distribution of the gas follows a Maxwell-Boltzman distribution with a mean velocity $\bar{v}$. The movement direction of each atom is randomly orientated. Let us also define the enthalpy H_0 in the stagnation chamber

$$H_0 = c_p T_0, \tag{2.14}$$

with the specific heat c_p for atoms

$$c_p = \frac{5}{2} k_B, \tag{2.15}$$

where is the Boltzman constant k_B. The expansion of the gas through the nozzle is driven by the pressure difference p_{vac}/p_0. In the nozzle, the (steady) gas flow becomes directed and the enthalpy H_0 is converted into kinetic energy $\frac{1}{2}mv^2$ and a rest enthalpy H. So, in the expansion process, we can use the conservation of energy, and equation (2.15) we can write down

$$H_0 = H + \frac{1}{2} m_{gas} v^2 = c_p T + \frac{1}{2} m_{gas} v^2, \tag{2.16}$$

with T being the local temperature along the gas flow and m_{gas} the atomic mass of the gas. To look at this in greater detail, let us define the Mach number M as the ratio of the stream velocity v and the local speed of sound c_s

$$c_s = \sqrt{\frac{\gamma k_B T}{m_{gas}}}. \tag{2.17}$$

With the ratio of specific heats $\gamma = \frac{c_p}{c_v}$ at constant pressure and volume, they can be regarded as independent of temperature for atomic gases, we can rearrange equation

2.16 to

$$T = T_0 \left(1 + \frac{1}{2}(\gamma - 1) M^2\right)^{-1}. \tag{2.18}$$

Here the interplay between the Mach number M^2 and the local temperature T give insight into the directed mass flow versus the remaining thermal energy in the system. As indicated the the figure 2.8, M increases dramatically along the expansion axis and that is due to decrease in speed of sound c_s that is proportional to $\sqrt{T}$ as indicated in equation (2.17)[9]. Finally, this attribute has given the name to supersonic jets.

Let us describe the appearance of the jet stream (see figure 2.8)next. Upon exiting the nozzle, the Mach number increases by a wide margin ($M \gg 1$), that means that the gas travels faster than information in this medium. Here, a *zone of silence* is formed, where the gas flow is not influenced by other particles, thus uninterrupted. As the supersonic flow is exiting the nozzle it has to turn around the edge of the nozzle to further expand and the supersonic flow turns by actually creating smaller Mach waves. At the borders of the *zone of silence*, M decreases drastically resulting in dense regions that are called *barrel shock* to the sides and *Mach disk* downstream the gas flow. For an unhindered transport of the gas and clusters to the interaction region, the interaction region needs to be within the *zone of silence.* We can express the distance from the nozzle to the Mach disk through

$$\frac{x_{MD}}{d} = 0.67 \left(\frac{p_0}{p_b}\right)^{\frac{1}{2}}. \tag{2.19}$$

So the the competing stagnation pressure p_0 and the background pressure p_b define the distance of the otherwise static parameters. Hence, p_b needs to be low enough do drive the Mach disk downstream of the interaction region. By using skimmers and physically separating the jet expansion into separately pumped compartments, the background pressure p_b can be reduced.

While we have described a cooling gas in the expansion process it should be noted that the clusters are comparably hot. Through the kinetic process described above, they are efficiently heated. The two processes to loose energy are, one, collisions with a chaperone M that deactivates the cluster, or two, evaporation of monomers from the cluster. The evaporation process makes the temperature size-independent, after the clusters have reached a certain minimum size [41]. It is tedious and experimentally difficult to measure the temperature exactly but typically, the jet reaches temperatures

---

[9] In other words, the gas is expanding and quickly reaches the terminal velocity $v_\infty = \sqrt{\frac{2R}{m_{gas}}\left(\frac{\gamma}{\gamma-1}\right)T_0}$, with R being the universal gas constant, while the speed of sound is decreasing. This can be abused to calculate flight times $t_{\text{flight}} = \frac{d}{v_\infty}$, if the distance d from nozzle to interaction point is known.

Helium	Neon	Argon	Krypton	Xenon
3.85	185	1646	2980	5554

Table 2.1: Parameter K values for rare gases [1].

of a few Kelvin and the cluster temperature is heavily dependent on their material, particular the dissociation energy. For this study relevant are mostly the temperature of Xenon cluster that is $75K$[10] and the fact xenon clusters are solid because their melting temperature is higher[42]. Follwing this same line of argumentation, helium clusters are liquid, which is why they are often called (helium-)droplets. If helium droplets are produced using a cryogenic jet even superfluid helium-droplets can be observed.

At the current point of the discussion, it should shine out that the average cluster size is very much depended on the gas type, stagnation temperature T_0, stagnation pressure p_0 and the nozzle type. Indeed, an empirically found scaling law named after Hagena [43–45], can be written down as

$$\Gamma^* = K \cdot T_0^{0.25q-1.5} \cdot p_0 \cdot d_{eq}^q, \tag{2.20}$$

with the gas specific parameter K that can be found in table 2.1 for some rare gases, the gas specific parameter q that varies between 0.5 and 1 and is 0.85 for all rare-gases, and the equivalent nozzle opening d_{eq} that is $d_{eq} = d$ for pinhole sources and for conical nozzles d_{eq} reads

$$d_{eq} = d\frac{\tan(\Phi_0)}{\tan(\Phi)} \tag{2.21}$$

with the half opening angle of the nozzle Φ and the half opening of the free gas expansion Φ_0. The Hagena scaling parameter Γ^* allows us to estimate the mean cluster size, i.e. amount of accumulated particles per cluster $< N >$, as follows

- $\Gamma^* < 350$, no cluster formation observed.
- $350 < \Gamma^* < 1800$, in this region $< N >$ reads

$$< N >= 38.4 \left(\frac{\Gamma^*}{1000}\right)^{1.64} \tag{2.22}$$

---

[10] To put this temperature in perspective, krypton clusters are $50K$ and argon cluster $40K$ [41, 42]. Note that in this study the cluster size was $\bar{N} > 800$, hence above the minum value to be size independent. For the evaporative cooling process to settle at a given temperature, a certain flight distance (in the cited study 6.5cm) should also be taken into account.

- $1800 < \Gamma^*$, in this region $< N >$ reads

$$< N >= 33.0 \left(\frac{\Gamma^*}{1000} \right)^{2.35} \tag{2.23}$$

Supersonic jets generally create clusters of different sizes. This size distribution is centered around $< N >$ and for solid rare gas clusters, this distribution is a log-normal distribution. The size distribution can be an experimental challenge, especially when size dependent effects are investigated. Historically, electron diffraction [41, 46] has been used to determine the mean cluster size, mean temperature and mean geometry. Today, free electron laser allow the determination of the size of a single cluster through a diffraction image and by measuring enough single clusters, one can reproduce size distributions of a supersonic jet as shown in figure 5.1.

Experiments using supersonic jets for cluster generation are typically performed with pulsed valves to decrease cost and gas load in the overall system. Upon opening and closing of the valve, the gas density varies. This mostly affects the cluster size and one would expect to see smaller clusters. This remains true in the beginning of the pulse but in the *afterpulse* one finds giant clusters that exceed the above described scaling laws [47].

2.2.2 Creation of a heterogeneous cluster

The creation of heterogeneous clusters as they have been used in this study stands in the foreground of this chapter. One of the possibilities to create heterogeneous clusters is through the principle of picking-up atoms or molecules [32, 48]. Figure 2.9 illustrates pickup regions that are typically used in an experiment. Mainly, there are two different pickup places, one, monomers are added to the cluster in region A of figure 2.9 that represents the nozzle of a supersonic source, or two, they can be picked up by a cluster in region B for example through an increase background pressure p_{b2} or a pickup gas-cell. If clusters pick up atoms or molecules in the nozzle region A, they can become part of the cluster formation and can be found inside of solid clusters. If atoms or molecules are picked up in region B, they stick to the surface of solid clusters. Since the traversing cluster is much larger and heavier than a colliding monomer the trajectory is not affected significantly. Already pressures of 10^{-11} bars over a pickup length of a few centimeters can dope the cluster in significant form. At these low pressures, picking up atoms or molecules in region B requires less gas load on the system but is also less efficient than picking up in region B. To increase the pickup levels in region B, a gas cell can be used

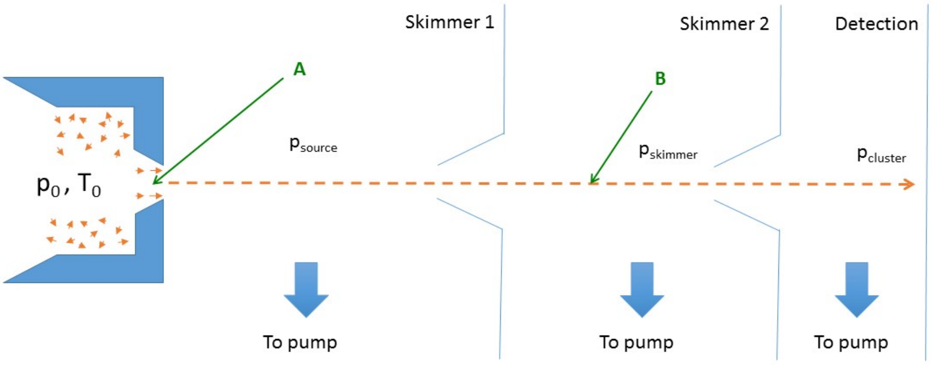
Skimmer 1
Skimmer 2
Detection
A
B
p_{source}
$p_{skimmer}$
$p_{cluster}$
p_0, T_0
To pump
To pump
To pump

Figure 2.9: Schematic setup to generate heterogeneous clusters through pickup. Thereby is a first cluster generated via a supersonic gas expansion, which is doped at regions marked A or B. In region A, the dopant gas is mixed in the nozzle such that it becomes part of the nucleus. In region B, the cluster condenses atoms on its surface and commonly gas cells are used to regulate the pressure p_{skimmer} effectively. p_{source} is the pressure in the source chamber. The cluster can be detected upon evaporation, i.e. by contact with the chamber, through the pressure p_{cluster} and the cluster doping can be determined through partial pressures (see text for details). After [32, 48].

as much higher pressures can be achieved within the gas cell without putting too much load on the overall system.

The collision with the cluster and a dopant does add energy to the cluster just as the cluster growth process itself. This is why the initial cluster will loose particles through evaporation upon pick up of a dopant [49]. The loss of particles through evaporative cooling is, proportional to the ratio in dissociation energies of the cluster and picked up material and reads

$$N_{\text{Evaporated from cluster}} \approx \frac{\epsilon_{\text{cluster}}}{\epsilon_{\text{dopant}}}. \tag{2.24}$$

In the case, where a helium droplet is doped with xenon atoms, we may use the dissociation energies of helium $\epsilon_{He} = 0.6 \cdot 10^{-3}$ eV and xenon $\epsilon_{Xe} = 0.6 \cdot 10^{-3}$ eV [49, 50], such that approximately 250 helium atoms evaporate by picking up 1 xenon atom.

We can extend this idea to estimate the amount of picked-up atoms, if we were to know the amount of atoms in the cluster before and after the pickup area. An estimate of the initial cluster size $\langle N_{\text{cluster}} \rangle$ can be reached through the scaling laws[11] as discussed in section 2.2.1. A measure to estimate the cluster size after the pickup can be established through measuring the partial pressure of the cluster material p_{cluster} of helium[12], when the particle jet hits a wall and evaporates (see figure 2.9). The partial pressure p_{cluster} scales then linearly with the initial cluster size $\langle N_{\text{cluster}} \rangle$, such that

$$\langle N_{\text{dopant}} \rangle \approx \frac{\epsilon_{\text{cluster}}}{\epsilon_{\text{dopant}}} \cdot \frac{\Delta p_{\text{cluster}} \langle N_{\text{cluster}} \rangle}{p_{\text{cluster}}}, \tag{2.25}$$

where $\Delta p_{\text{cluster}}$ denotes the partial pressure difference with pickup and without.

2.3 Introduction into X-ray scattering

This section will give a brief introduction into the elastic scattering of X-rays with matter. The actual scattering process is very complex as it is an interplay of coherent, incoherent and elastic, inelastic processes. Fortunately, we can reduce the scattering description to its main process: The coherent and elastic scattering. In other words, we neglect Compton scattering (incoherent), any kind of absorption processes (inelastic) and effects form the scattering of multiple particles. We will then start this section by looking at the small angle scattering of atoms and continue on to extended objects such as clusters. The section is rounded off by an introduction to the inverse problem and basic algorithm ideas to overcome the issue of phase retrieval.

---

[11] As already established the actual cluster size produced with a supersonic jet will vary, hence the average cluster size $\langle N_{\text{cluster}} \rangle$.

[12] For example with a residual gas analyzer.

2.3.1 Small angle X-ray scattering

We can describe a linear polarized, electric field of a continuous electromagnetic wave via the following expression [5]

$$\vec{E}(\vec{r},t) = \vec{\epsilon} E_0 e^{i\vec{k}\cdot\vec{r}}, \tag{2.26}$$

with $\vec{E}(\vec{r},t)$ being the electromagnetic field of the wave, the wave vector $\vec{k}$, the Cartesian coordinate vector $\vec{r}$, the complex amplitude if the electric field is then $E_0 \exp^{i\vec{k}\cdot\vec{r}}$ and because of the polarization we use $\vec{\epsilon}$ such that $\vec{\epsilon}\cdot\vec{k} = \vec{k}\cdot\vec{E} = \vec{k}\cdot\vec{H} = 0$. If this wave encounters an electron, we can describe the scattering semi-classical by imagining how the electric field of the electron starts to oscillate once it sees an incoming electric wave. The electron then functions as a dipole antenna eventually radiating the wave into a certain solid angle $\Delta\Omega$. Through a relative comparison, of the incoming intensity and the scattered intensity, we can phenomenological establish the differential cross-section as

$$\left(\frac{d\sigma}{d\Omega}\right) = \frac{(\text{Number of X-rays scattered per second into } \Delta\Omega)}{(\text{Incident flux})\,(\Delta\Omega)} = \frac{I_{sc}}{(I_0/A_0)\,\Delta\Omega}, \tag{2.27}$$

with A_0 being the covered area of the incident beam. And depending on the polarization of the incident beam we can reduce equation 2.27 to

$$\left(\frac{d\sigma}{d\Omega}\right) = r_0^2 P, \tag{2.28}$$

with the classical electron radius $r_0 = 2.82\ 10^{-5}$ Åand the polarization factor P

$$P = \begin{cases} 1 & \text{vertical scattering plane,} \\ \cos^2(\Psi) & \text{horizontal scattering plane,} \\ \frac{1}{2}\left(1+\cos^2(\Psi)\right) & \text{unpolarized source.} \end{cases} \tag{2.29}$$

We can now move on and use this knowledge for atoms, where we have Z electrons. To describe electrons in an atom, let us proceed purely classical by introducing the electron density $\rho_e(\vec{r})$ that describes the distribution of electron in an atom on average. Now, figure 2.10 illustrates the scattering process in one atom. An incident beam with wave number $\vec{k}$ is elasticity scattered at a point $\vec{r}$ into a wave with $\vec{k}'$ such that $\left|\vec{k}\right| = \left|\vec{k}'\right|$. In this wave picture, the scattering process must be seen as a superposition of waves and it is particular illustrated how the wave scattered at the origin of the atom is scattered as well. As both waves are scattered at different points, they have an optical path difference 2δ. This difference in path length results in a phase difference to each other and eventually leads to interference between the waves. So, we can describe the phase difference $\Delta\Phi\left(\vec{r}\right)$ of the waves scattered at $\vec{r}$ and the origin by

$$\Delta\Phi\left(\vec{r}\right)=\left(\vec{k}-\vec{k}'\right)\cdot\vec{r}=\vec{Q}\cdot r, \tag{2.30}$$

with $\vec{Q}$ being denoted as the *wave-vector transfer*. Through trigonometry, we can then establish the more common denotation of the wave-vector $\vec{Q}$

$$\vec{Q}=2\left|\vec{k}\right|\sin\left(\Theta\right)=\frac{4\pi}{\lambda}\sin\left(\Theta\right), \tag{2.31}$$

with the wavelength of the light λ and the scattering angle Θ.
A volume element $d\vec{r}$ at $\vec{r}$ will now scatter depending on its electron density, namely by $-r_0\rho\left(\vec{r}\right)d\vec{r}$. At scattering angle 0, i.e. $\vec{Q}=0$ the atomic form factor f^0 is

$$f^0\left(\vec{Q}\rightarrow 0\right)=Z, \tag{2.32}$$

as all scatter are in phase. As we increase the scattering angle Θ, the phase difference $\Delta\Phi\left(\vec{r}\right)$ leads to interference and we can describe this via a phase factor $e^{i\vec{Q}\cdot\vec{r}}$, hence $f^0\left(\vec{Q}\rightarrow\infty\right)=0$. If we integrate over the total scattering length, we can then write down

$$-r_0f^0\left(\vec{Q}\right)=-r_0\int\rho_e\left(\vec{r}\right)e^{i\vec{Q}\cdot\vec{r}}d\vec{r}. \tag{2.33}$$

The atomic form factor can hence be seen as a Fourier transform of the classical electron density of an atom. To make it more clear, (X-ray) diffraction projects an image of the atom in reciprocal space.
Let us continue with the scattering of a molecule or cluster. We can label the atoms in such a particle by

$$F^{object}\left(\vec{Q}\right)=\sum_j f_j^0\left(\vec{Q}\right)e^{i\vec{Q}\cdot\vec{r}}, \tag{2.34}$$

with the atomic scattering factors $f_j^0\left(\vec{Q}\right)$ for the j'th atom and call $-r_0F^{object}$ the scattering length of a cluster. Strictly speaking, $F^{object}\left(\vec{Q}\right)$ is angle depended, however, in the angular range of $\vec{Q}$, where $F^{Object}\left(\vec{Q}\right)$ is not 0, $f_j^Q\left(0\right)$ can be considered constant [see 51, p. 6-7]. In human hemoglobin, the range in which the molecule scattering length

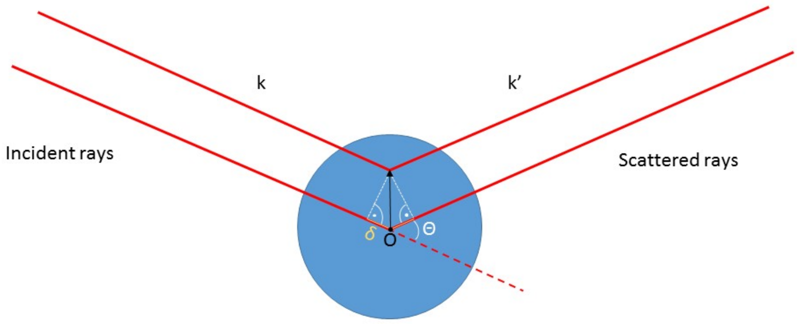

Figure 2.10: Principle of scattering rays of an atom. After [5, 51].

is not 0, the carbon atomic scattering factors change less than 0.4%. It is therefore most convenient to describe the scattering of extended objects via a continuous electron density, where certain volume elements $d\vec{r}$ scatter proportional to their electron density $\rho_e\left(\vec{r}\right)$. We can therefore go forward with a continuous description of extended objects using a generalized electron density $\rho\left(\vec{r}\right)$.

Let us summarize this briefly by recalling from optics in general that a lens is performing an inverse Fourier transformation to project the scattering from an object as a realspace image. Through expressing the probability of presence of an electron in the scattering process through a general electron density $\rho\left(\vec{r}\right)$ of an object. The reason why this is important is that free electron laser are the first light-sources to have enough photons in just one light pulse to generate a snapshot of a nanometer-sized particle, e.g. a biomolecule, in just one shot. The total scattered intensity $I\left(\vec{Q}\right)$ in a measurement is

$$I\left(\vec{Q}\right) = |A|^2 = I_0 \left|F^0\left(\vec{Q}\right)\right|^2, \qquad (2.35)$$

with the incident beam intensity I_0, the (complex) amplitude A and

$$F^0 = \int \rho\left(\vec{r}\right) e^{i\vec{Q}\cdot r} d\vec{r}. \qquad (2.36)$$

Clusters can be considered as spherical symmetric and if we assume such an electron density density $\rho\left(\vec{r}=\{0,..,R\}\right)=1$ of a particle with radius R, we solve the integral in equation (2.36) through transforming into spherical coordinates

$$F^0_{Sphere}\left(\vec{Q}\right) = \int_0^{\pi}\int_0^{2\pi}\int_0^{R} r^2 sin\left(\Theta\right) e^{iQr\cos(\Theta)} dr d\Theta d\Phi \tag{2.37}$$

$$= \frac{\sin\left(\vec{Q}R\right) - \vec{Q}R\cos\left(\vec{Q}R\right)}{\vec{Q}^3R^3} = \frac{J_1\left(\vec{Q}R\right)}{\vec{Q}R}, \tag{2.38}$$

with J_1 being the Bessel function of first kind. Formula (2.38) can be easily abused to determine the size of a spherical particle using the local minima in the diffraction pattern.

The process of measuring the scattered light, e.g. through a detector, one merely measures the modulo of an amplitude $|A|^2$, which eliminates the phase factor $e^{i\Delta\Phi(\vec{r})}\cdot e^{-i\Delta\Phi(\vec{r})}=1$. In order to reconstruct the object that scattered in realspace, e.g. to understand its shape or to study its function, we need to recover this phase information. We will discuss this briefly in the next section.

2.3.2 The inverse problem: Phase retrieval

The loss of the phase in the scattering process results ultimately in a sign problem. The scattered intensity $I\left(\vec{Q}\right)$ is proportional to the form factors $\left|f^0\right|^2$. To recover the phase and thus reconstruct the particle iterative algorithms have been developed [52]. Figure 2.11 illustrates such an iterative algorithm, where the image of an object $g_k\left(x\right)$ is Fourier transformed to reciprocal space $G_k\left(x\right)$ and then back again resulting in $g_{k+1}(x)$, while sufficing certain criteria.

The constraints are rather strict define in the reciprocal space as they have to reproduce the actual measurement $I=A\cdot A^*$. The constraints that need to be met can be chosen more freely. Generally, the recovered object should be physical, i.e. consist of positive values or should be of a certain (known) size. In simplified terms, one can introduce a support structure S that meets the physical criterion and can therefore be used to, for example, zero outling values. Throughout the iterations the functions $g_k(x)$ evolve and eventually converge into a solution. If one uses the above criterion, one can show that the error between the reconstructions and the actual measurement continuously reduces, which is why it is commonly referred to as error-reduction algorithm [53].

It should be noted that there is a great variety of manipulations that can be done upon not fulfilling a realspace constraint and although their function is fairly similar there is

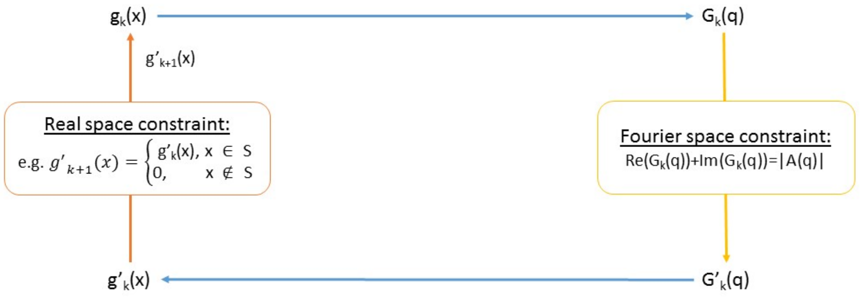
g_k(x)
G_k(q)
g'_{k+1}(x)
Real space constraint:
e.g. g'_{k+1}(x) = { g'_k(x), x ∈ S; 0, x ∉ S }
Fourier space constraint:
Re(G_k(q))+Im(G_k(q))=|A(q)|
g'_k(x)
G'_k(q)

Figure 2.11: Principle of a phase retrieval algorithm. The real space object $g_k\left(x\right)$ is Fourier transformed to $G_k\left(q\right)$. The function $G_k\left(q\right)$ is altered to fit the constraints set in Fourier space, hence $G'_k\left(q\right)$. $G'_k\left(q\right)$ is inverse Fourier transformed to $g'_k\left(x\right)$. After fulfilling the real space constraints the iterative starts again using $g_{k+1}\left(x\right)$. From [52].

a great variety of algorithms. Worth mentioning is the hybrid input-output (hio) [53] and the relaxed averaged alternating reflection (RAAR) [54].

2.4 Light-matter interaction

Photons can also be absorbed by atoms in which case an electron get either excited to another state or ionized. At X-ray wavelengths matter typically gets ionized in the inner shells. Upon absorption a cascade of relaxation processes begins and the now ionized atom finds the new most energetic favorable state. These processes are particularly depended on the wavelength of the incident photons but also the type of atom. This chapter is devoted to these processes and particular the absorption process is described in section 2.4.1 and the relaxation processes in 2.4.2.

2.4.1 Ionization of matter

Let us quickly remember the atomic scattering factor $f^0\left(\vec{Q}\right)$, which we were able to introduce by neglecting a variety of (wavelength depended) effects through Fourier transforming the electron density of an atom. If we imagine (soft) X-rays approaching an atom classically, we can compare it to the analogon to a forced harmonic oscillator, where an electric field drives a (bound) electron. As a result, the phase velocity of light v_{phase} is reduced to the speed of light in vacuum c through interacting with electrons. Hence we would think of an increase in the refractive index $n = c/v_{phase}$. Also, if the the energy of the photons is higher than binding energies of electrons in the atom then also a probability for dissipation/absorption exists [5, 55]. These two effects are connected to the atomic scattering factors $f^0\left(\vec{Q}\right)$ and are called dispersion corrections to the atomic scattering factor. Let us include these corrections as a atomic form factor

$$f\left(\vec{Q},\hbar\omega\right) = f^0\left(Q\right) + f'\left(\hbar\omega\right) + if''\left(\hbar\omega\right), \tag{2.39}$$

where $f'\left(\hbar\omega\right)$ corrects for the phase velocity and the wave amplitude correction/absorption $f''\left(\hbar\omega\right)$. In the limit of high photon energies $\hbar\omega$ the electrons can be largely seen as free, as the binding energies become a little factor, and $f'\left(\hbar\omega\right) \to 0$ and $f''\left(\hbar\omega\right) \to 0$. As the photon energies $\hbar\omega$ are closer to the atomic level, which is the case at soft X-rays for many materials, $f'\left(\hbar\omega\right)$ and $f''\left(\hbar\omega\right)$ can become large factors. Note particularly that these corrections only apply to the forward scattering, where $\vec{Q} = \Theta = 0$.

We shall not derive this relation in its full extend that can be read in [see 55, p. 55ff], but we shall compare the equation for the complex refractive index $n\left(\omega\right)$ to these arguments.

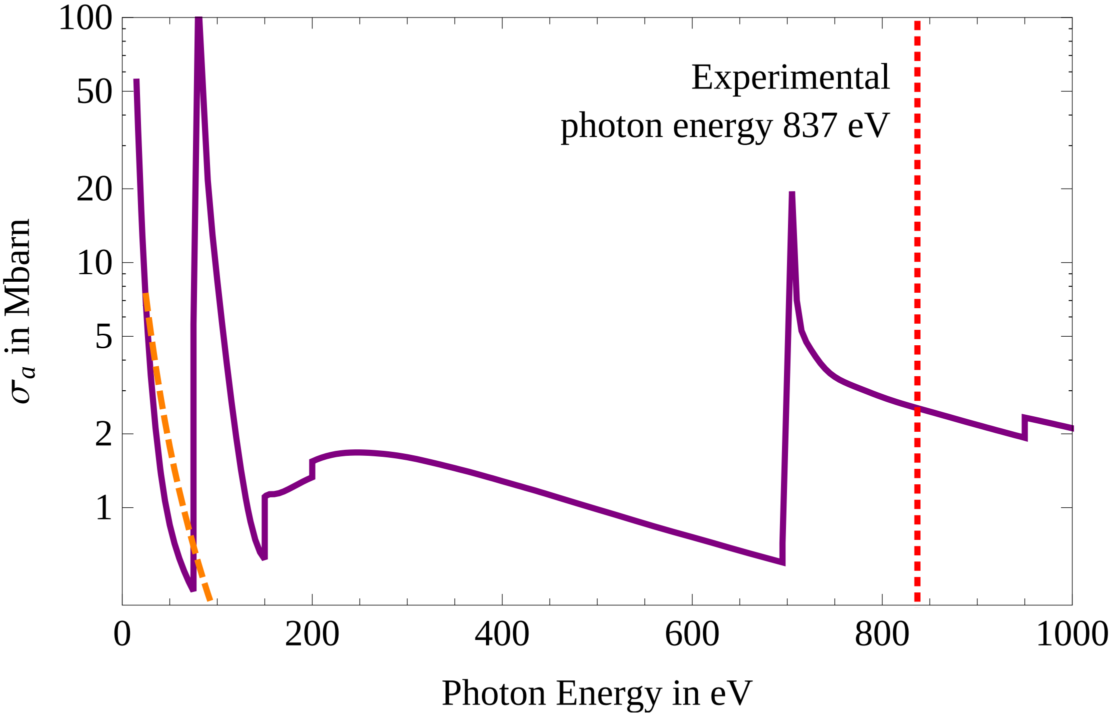

Figure 2.12: Total absorption crosssections σ_a in megabarn for xenon and helium. The purple curve represents the total cross-section of xenon. The orange dashed curve represents the total cross-section of helium. The red dashed line represents the photon energy used at the experiment described in the present work. Data points from [56–58]

Let us start by imagining a electromagnetic wave propagating in a medium. The wave propagating in a medium along the axis z can be written as

$$e^{inkz} = \underbrace{e^{i(1-\delta)kz}}_{\text{phase shift}} \underbrace{e^{-\beta z}}_{absorption} , \tag{2.40}$$

where n is the complex refractive index, δ the real dispersion correction resulting in a phase shift of the wave and β being the imaginary dispersion correction resulting in a decline in amplitude of the wave[13]. The relation between the complex refractive index, β and δ is explicitly given by

$$n \equiv \frac{c}{v_{\text{phase}}} = 1 - \delta + i\beta. \tag{2.41}$$

---

[13] We jump between wave and particle picture as it pleases us. Here, a decline in amplitude in the wave picture can be read as absorption in the particle picture.

Let us now jump to the result of the forced harmonic oscillator calculation given in [5, p. 278] and realize that we are allowed to define this dispersion relation through the atomic form factor as [see 5, p. 76]

$$n \equiv 1 - \frac{2\pi \rho_{atom} r_0}{k^2} \left(f^0 \left(\vec{Q} = 0 \right) + f' \left(\hbar\omega \right) + f'' \left(\hbar\omega \right) \right), \tag{2.42}$$

with the atomic number density ρ_{atom} and we identify

$$\delta = \frac{2\pi \rho_{atom} r_0}{k^2} \left(f^0 \left(\vec{Q} = 0 \right) + f' \left(\hbar\omega \right) \right), \quad \text{and} \tag{2.43}$$

$$\beta = -\left(\frac{2\pi \rho_{atom} r_0}{k^2} \right) f'' \left(\hbar\omega \right). \tag{2.44}$$

We have already established that β reduces the amplitude of the incoming wave through absorption. Thus, using the insight gained from the absorption part in equation (2.40), we can rewrite equation (2.44) and define $f'' (\hbar\omega)$ in terms of being proportional to an absorption cross section σ_a, which reads

$$f'' \left(\hbar\omega \right) = -\left(\frac{k}{4\pi r_0} \right) \sigma_a. \tag{2.45}$$

Figure 2.12 shows the total absorption cross-sections σ_a for xenon, helium under which a bound electron absorbs a photon and excited into the continuum, thus the atom is ionized. To get a better understanding of the fundamental absorption related details about xenon and helium, table 2.2 and 2.3 show the differential photo-absorption cross sections and ionization potentials for various energy levels and each ionization configurations, respectively, at the photon energy 837 eV. The calculations were performed using the Los Alamos Atomic Physics code based on [59]. It appears that certain energy levels, or here subshells if one disregards the hyperfine structure[14], tend to have a higher absorption cross-section than others. This brings us back to the picture of the forced harmonic oscillator, where an electron is driven by a light field. If the frequency of the light field is close to the eigenfrequency of the bound electron, in other words, if the energy of a photon is close to the energy level of a bound electron, the system is in resonance and absorption is highly likely. As the photon energy and electron level energy differ, the system is off resonance and it is less likely to absorb a photon. As energy levels in atoms are discrete, electrons can only be excited from one energy level to another or need a certain (minimal) ionization energy to ionize an atom and excite an electron into the continuum. The likelihood of a core-electron that is strongly bound

---

[14] A shift in energy levels due to interaction of electrons with the nucleus [see 60, p 166 ff.].

Shell	Subshell	Cross-section σ_a in Mb	subshell ionization potential in eV
K	1s	-	34630.0
L	2s	-	5466.4
	2p	-	4899.1
M	3s	-	1153.3
	3p	-	965.4
	3d	2.2505	682.7
N	4s	0.0305	223.7
	4p	0.1247	161.8
	4d	0.2587	68.2
O	5s	0.0040	27.3
	5p	0.0120	12.5

Table 2.2: Differential absorption cross-sections σ_a and ionization potentials for certain electronic configurations of xenon at 837eV. Calculations based on [59].

El. Configuration, and ionized subshell	Ionization of subshell	Cross-section σ_a in Mbarn	subshell ionization potential in eV
He^{+0}, 1s2	1s2	0.0007	24.4
He^{+1}, 1s1	1s1	0.0005	54.4
Xe^{+0}, 5p6	3d10	2.2505	682.7
Xe^{+1}, 3d9	3d9	2.1487	733.6
Xe^{+1}, 5p5	3d10	2.2443	693.7
Xe^{+2}, 5p4	3d10	2.2390	705.9

Table 2.3: Differential absorption cross-sections σ_a and ionization potentials for certain electronic configurations, including certain ionization profiles. Calculations based on [59].

being ionized is by far the most probable using X-rays. When a core electron gets ionized, the electronic structure changes and particular ionization energies and (absorption) cross-sections change. To discuss the parameters that are most applicable to this thesis, a comparison of the most probable transition at the photon energy 837eV is given for helium and xenon in table 2.3. The ionization energies change drastically, whether one ionizes are core electron or a less tight bound electron. Similarly to the back-on-the envelope calculation given in equation (2.2), it is very unlikely to an atom to absorb more than two photons in one pulse of a free electron laser, which is why we only consider the most probably transitions here to get an understanding how the absorption cross-sections change.

The total elastic scattering cross-sections for neutral and ionized helium and xenon can

El. Configuration, and ionized subshell	Scattering factor f^0 in barn
He^{+0}, 1s2	2.5539
He^{+1}, 1s1	0.649465
Xe^{+0}, 5p6	1874.36
Xe^{+1}, 3d9	1813.56
Xe^{+1}, 5p5	1814.68
Xe^{+2}, 5p4	1754.08

Table 2.4: Elastic scattering factor f^0 for certain electron configurations. Calculations based on equation (2.33). From [61]

be found in table 2.4. It is interesting to see that although xenon has only 27 times more electrons than a helium atom the scattering factor f^0 of neutral xenon is over 900 times stronger helium. Upon ionization, the absolute changes in f^0 of helium are therefore smaller compared to xenon. However, the relative change in helium of f^0 by getting one of two electrons ionized 75% and ionized helium barely scatters. As xenon has multiple occupied subshells, the scattering factors of different ionized subshells are shown. As discussed, it is most likely to ionize the 3d subshell but subsequent relaxation processes[15] lead to a ionized 5p subshell. For the scattering factor, there is little change whether the 3d or 5p subshell becomes ionized and the change in f^0 is only 0.05%. As xenon has 54 electrons, the relative change upon ionization of one electron in f^0 is only 3% and small compared to helium, which allows us to conclude that xenon scatters still well after ionization. In the experiment described in the following chapters, the photon energy is explicitly chosen to have a comparably high absorption cross-section for xenon but is off absorption resonance, a comparably low absorption cross-section for helium and a wavelength short enough to receive high resolution images through coherent diffraction imaging. In such a setting xenon is most likely to absorb X-rays rather than helium. Thus given the raw absorption likelihoods, the xenon atoms (and clusters) are most prone to X-ray induced dynamics. Let us now have a look at these dynamics in atoms and study the electronic relaxation processes in atoms upon absorption of an (X-ray) photon.

2.4.2 Charge migration

After an atom has been (core-)ionized due to absorption of a photon as depicted in figure 2.13a, the atom is not in its most energetically favorable state. In order to emit

---

[15] See the following section 2.4.2.

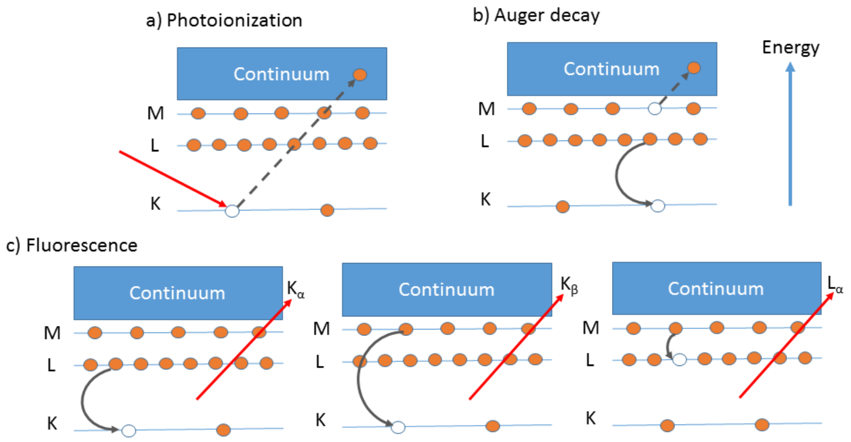
a) Photoionization
b) Auger decay
Energy
Continuum
M
L
K
c) Fluorescence
K_α
K_β
L_α

Figure 2.13: Schematic illustration of common charge transfer processes. a) describes a direct emission of an K-shell electron after absorbing a X-ray photon. Process b) shows a secondary relaxation process called Auger decay, where a K-shell hole is filled with an electron from the L-shell and the remaining energy is released through emission of an electron in an outer shell, here M-shell, into the continuum. Process c) illustrates fluorescence, where an electron hole is filled with an electron from an outer shell and the remaining energy is released through photons. Process a) has a destinct spectra depending on the ionized element and the wavelength of the absorbed photon, the released particles in b-c) show an element specific spectra. After [5, p. 19]

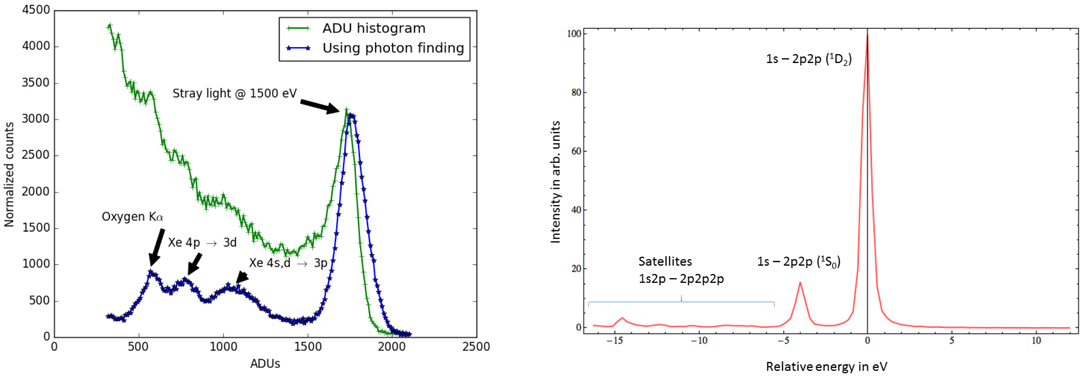

Figure 2.14: Left spectra shows fluorescence peaks from xenon and oxygen illuminated with 1.5keV photons from the LCLS and detected with pnCCD detectors [62, 63]. The green curve is a ADU histogram of the pnCCD detector and the blue curve uses a coalescent photon finder as described in section 4.2. Right, selection of the K-LL Auger spectrum with rel. energy 0 corresponding to 804.5eV. The ionization starts in the K shell, i.e. a 1s hole, and the Auger relaxation process ends up with two holes, e.g. in the L-shell denoted as LL or 2p2p. As electrons energy levels arrange due to their quantum numbers, multiple peaks appear for similar hole configurations, e.g. 2p2p [18, 64].

energy and transition into its new ground state, the atom can emit particles according to the schematics in figure 2.13b-c. The electron hole in the (K-)shell created due to absorption of a photon above ionization threshold is filled by an electron in a energetically higher shell, here L or M shell, and thereby emits a photon of the discrete energy of the difference between the transitioning levels. The discrete lines are thus element specific and modern photoemission spectroscopy can yield insight into for example element identification, excitation dynamics or chemical bonds. Figure 2.14 left shows measured fluorescence lines of oxygen and xenon. In this measurement, xenon atoms and residual oxygen atoms have been illuminated with 1500 eV photons from the Linac Coherent Light Source and the fluorescence photons has been measured with the LAMP pnCCD detectors described in section 3.3. The green curve is a ADU histogram of the pixel-detector using the detector calibrations described in section 4.2. The blue curve additionally uses a photon-finding algorithm as the signal from just one fluorescence photon splits up into multiple pixel. An algorithm then looks for pixel above a certain threshold and includes neighboring pixel above a certain threshold, thus correcting the measured signal to yield a proper fluorescence yield.

Another possibility for the atom to emit absorbed energy is through a 2-step process, where an outer shell electron is emitted into the continuum, the so called Auger-electron[16] and simultaneously another electron fills the electron-hole. Emitted Auger-electrons have discrete energies depending on the combination of electrons involved in the process and can therefore help identifing elements or be used to calibrate energies. Figure 2.14 right shows a partial K-LL Auger spectrum from neon illuminated by soft X-ray pulses from LCLS and measured with a hemispherical analyzer as described in [18]. Neon is ionized in the K-shell and electron-hole in 1s is created. In the Auger decay, an electron from the L-shell fill the 1s hole and another electron from the L-shell is emitted into the continuum. As there is a variety of electronic configurations that can be involved in this process multiple peaks appear for similar configurations, e.g. 1s - 2p2p. More complex structures, called satellites, appear when the initial ionization configuration is more complex, e.g. KL-LLL satellites. An Auger decay occurs typically on the few femtosecond timescale [64].

Similar to the Auger decay, where electrons from an outer shell are involved in the relaxation process, the transition can also be of the same shell and is then called a Coster-Kronig transition. Relevant transitions are for example the N-NN Coster-Kronig transitions in xenon [**?**].

So far we have looked at X-ray induced processes from atoms. Extended objects, whether a bio-molecule or a cluster, will respond differently than just the atoms they consist of. Nanometer-sized objects will develop a distinct character due to their electronic bond with other particles. This includes rare-gas clusters that are weakly bound Van der Waals forces. We shall explore this behavior in the next section 2.5.

2.5 Ionization of clusters in intense X-ray pulses

The response of a cluster in intense X-rays differs from just the atomic response. Collective effects change the microscopic (sample) environment and it is now the collective of atoms that generates a response to the strong FEL pulse.

2.5.1 Formation and expansion of a nanoplasma

Let us begin by recapture the elastic, coherent scattering part of the response that has been discussed in section 2.3. Equation (2.34) indicates how the scattering length of a cluster can be calculated and, neglecting inelastic processes, this remains elastic scattering response holds true. If we consider the inelastic effects discussed in section

---

[16] Named after the french physicist Pierre Auger.

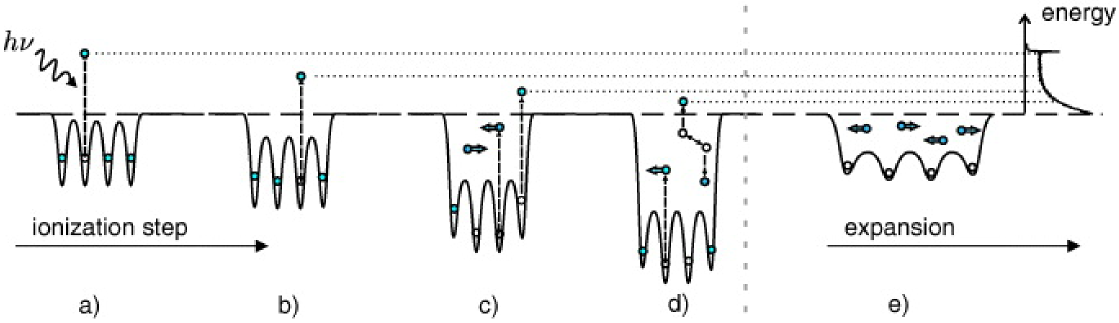

Figure 2.15: Schematic illustration of the nanoplasma creation and expansion. In step a) X-ray photons ionize electrons from a cluster. b) subsequent *multi-step ionization* try to relax the electronically excited system, deepening the Coulomb potential of the cluster. Step c) shows a deepened Coulomb potential of the cluster, due to which the multistep ionization becomes (partially) frustrated and electrons are trapped in the potential. In step d) trapped electrons collide and start to thermalize. Collisions can lead to emission of trapped electrons. d) The superheated nanoplasma starts to expand. From [65, 🅭🅯]

2.4.1, it should be clear that the elastic scattering length -$r_0 F^{Object}$ is reduced due to the (atomic) dispersion corrections $f'(\omega)$ and $f''(\omega)$ that reduce the scattering length $-r_0 f^0\left(\vec{Q}\right)$ of a single atom. The dominating change in scattering length is driven by the photo ionization process introduced via $f''(\omega)$. We follow the figure 2.15 and [65, 66] in the next five steps. Step a) of the nanoplasma transition, the cluster gets ionized due to intense radiation[17]. Step b), further ionization through emission of photo electrons and Auger electrons lead to a so called *multistep ionization* that steepens the Coulomb potential [67–69]. Step c), the multistep ionization is suppressed (or frustrated) because the Coulomb potential depth is larger than the atomic excess energy of photo- and Auger electrons. The emitted electrons are now trapped in the cluster potential and are *quasi-free.* Upon increasing *inner ionization* the nanometer sized object undergoes a phase transition to a nanoplasma[18]. Step d), the temperature of the nanoplasma is initially defined by the atomic excess energies (a rather discrete spectrum) but collisions with other particles lead a (kinetic) energy distribution of the electrons that is similar to thermal distributions and can be measured via the spectra of evaporated electrons [70, 71]. Step e) Hydrodynamic and Coulomb forces drive an expansion of the cluster and the cluster will ultimately disintegrate. The hydrodynamic portion of the force is due to the increasing hot plasma and the resulting increase outward pressure, whereas the the Coulomb portion comes from the repelling force of same charges. Both these forces reasonably describe the expansion process, are not exclusive and depend mostly on sample size and irradiation technique.

---

[17] The wavelength of radiation must be above the ionization threshold of at least one subshell, however, it must not be X-rays with a wavelength on the nanometer length scale.

[18] Plasma is another state of matter, similar to solid, liquid and gaseous, where molecular bonds dissociate and positive and negative particles are present in increasing numbers.

Regarding the sample size, large clusters efficiently trap electrons in their Coulomb potentials such that the quasi-free electrons thermalize and subsequently heat the nucleus. The hot nanoplasma system then tries to expand due to the increase in internal pressure. Electrons thermalize on the attosecond timescale and simulations show that the energy transfer to the ions can be as fast as 50 fs [72]. Small clusters trap photo and Auger electrons less efficiently and electrons are free such that the heating process is suppressed. In this case, the ions see the repelling force due to Coulomb interaction of same charges with each other [73].

Following a similar line of argumentation, low energy ionizing photons allow efficient trapping of photo and Auger electrons, thus favorable conditions for a hydrodynamic expansion. Conversely, high photon energies[19] lead to more atomic excess energy such that more electrons overcome the trapping potential, thus favorable conditions for a Coulomb expansion. However, this line is very element depended and atoms with large atomic mass, such as Xenon[20] would require photon energies E_{ph} of $5.5keV \ll E_{ph} < 34.6keV$ or $34.6keV \gg E_{ph}$ and since mostly the immediate process upon photon absorption is wavelength depended and the electron trapping of the majority of subsequent multistep ionizations will be mostly depended on the cluster size. It remains to discuss the radiation intensity and the more intense the ionizing radiation is, the more electrons are ionized per time-step such that the intensity of the light mainly drives the time needed for a cluster to undergo the phase-transition to a nanoplasma, expand and disintegrate.

2.5.2 Imaging of transient states

The reason why the nanoplasma transition is important is because every matter irradiated by a free-electron laser will undergo the nanoplasma transition and finally disintegrate. This is particular challenge for structural biology [75] as sample damage due to the FEL x-ray pulse changes the desired structure one ought to investigate. In order

---

[19] Meaning hard X-ray with wavelenghs on the Ångstrom length scale as soft X-rays have similar photon energies as trapping potentials and multistep ionization deepens the Coulomb potential enough.

[20] Find ionization energies for specific subshells in table 2.2 and deepened Coulomb potential ionization energies after ionization of Xe, here $Xe^{+}1$ and Xe^{+2} for different subshell ionization configurations, in table 2.3.

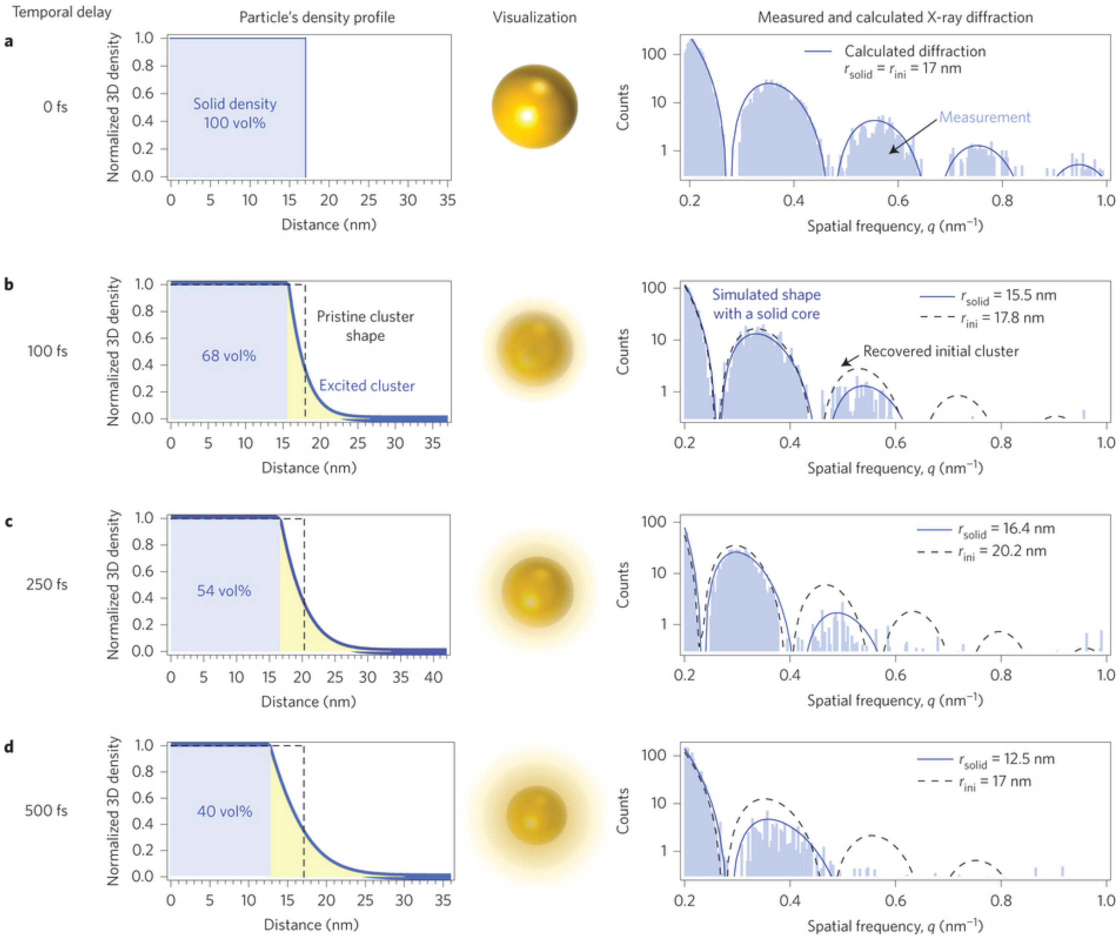

Figure 2.16: Left series, simulation of of diffraction patterns. Right series, measured diffraction patterns of (spherical) xenon clusters pumped with an NIR laser pulse and probed a certain time delay with an LCLS pulse. The diffraction pattern show a decrease in intensity at larger q values, which can be explained through an expanding electron densities, i.e. a nanoplasma expansion. Electron density simulations are performed in 1D and the densities Fourier transform is fitted to the measurement for a solid sphere (dashed line) and an expanding sphere (solid line). From [74]. Reprinted with permission from Nature Publishing Group.

to prevent falsified measurements, one needs to understand the nanoplasma transition as it occurs while the pulse is propagating through the sample. First attempts to perform a combined spectroscopic and imaging technique revealed correlations between the complex refractive index [76] and the diffraction patterns but also correlations of the ion spectroscopic data and the diffraction patterns intensity [77]. More recently, simulations on diffraction patterns could show the expanding electron density [74] as it is also shown in figure 2.16. In this particular study, an infra-red laser was used start (pump) a nanoplasma transition in a xenon cluster and subsequently image (probe) this state with a XFEL pulse. As the time delay between pump and probe pulse is varied, the resulting diffraction patterns of the 15-20 nm Xe-cluster show declining intensities at larger scattering angles with increasing time delay $\Delta t > 100fs$. The loss in signal could be explained through an expanding electron density [78, 79]. The electron density thereby expands increasingly over time due to the Coulomb and Hydrodynamic forces and, first the outer layers expand and at larger time delay also the inner atomic layers. In this study, an electron temperature of 200eV could be measured in this study by comparing plasma simulations to the ion spectroscopy signal. The possible spatial resolution out of the diffraction patterns has been estimated to be 8 nm but through assuming a shape the electron density model is sensitive below this resolution.

At shorter time delays $\Delta t < 100fs$ xenon cluster compress in size [29]. Since clusters form as a crystal[21], one can determine their structure through crystallographic approaches as it is explained in full detail in [5, chapter 5][22]. Figure 2.17a is showing how the signal from fulfilling Bragg's law over the scattering vector q. The signal moves to larger scattering vectors q and, as $q = \frac{2\pi}{a}$, the unit cell length a is shrinking over the time delay $\Delta t = \{0, .., 100\}$. This unintuitive and contradictory result is attributed to the changes in electronic configuration upon ionization. Electrons that are trapped in the cluster Coulomb potential have an increased mobility and are able to contribute comparable to valence electrons to the chemical bonding. As a result, the unit cell, i.e. the crystalline structure, changes on the Ångstrom length scale and the lattice becomes increasingly disordered (see figure 2.17c). Conversely, this stand in stark contrast with the experiment explained above. The nanoplasma transition is therefore a multistep process in which first the initial ionization occurs, followed by an increased Coulomb potential

---

[21] See section 2.2.1.

[22] In short, crystals scatter light and through interference when fulfilling the, so called, Bragg-law $m\lambda = 2d\sin(\Theta)$, with m being an integer, λ being the wavelength of the scattered light, d the distance between crystalline layers and Θ the scattering angle. When Bragg's condition is fulfilled, the rays interfere constructively and signal can be detected. Similar to small angle scattering, the image of the crystal is best expressed in reciprocal space where d can be connected to a and Θ to q (or $\vec{Q}$ as denoted earlier) such that a structure can be determined.

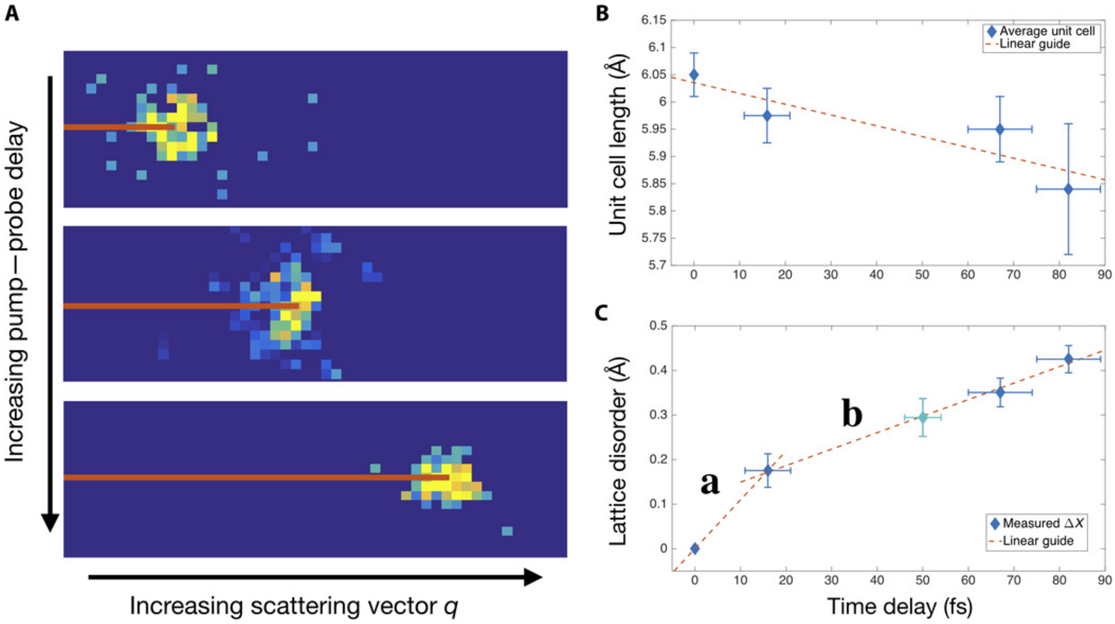

Figure 2.17: X-ray pump – X-ray probe scattering experiment on Xe-cluster that shows an early evolution of the nanoplasma transition. A, single-shot Bragg peaks at varying time delays. The scattering vector q increases over time delay. B, unit cell length over time delay. The unit cell length decreases, therefore the cluster shrinks in size. C, Lattice disorder over time delay. The measured fcc lattice is becoming disordered after being pumped with a X-ray pulse. From [29]. Reprinted with permission from AAAS.

that traps electrons, which then change the structure of the nanosample. Eventually, the system becomes strongly ionized and hot such that Coulomb and hydrodynamic forces disintegrate the cluster into it's atomic components.

2.5.3 Tampered layers to inhibit the nanoplasma expansion

Initially, it was proposed that very short pulses outrun radiation damage processes [75]. Pulses from the XFEL must be shorter than the lifetime of Auger processes, thus on few femtosecond long, to outrun the multistep ionization. It shall also be noted here that limiting the XFEL pulse duration, e.g. at LCLS, limits the pulse energy and therefore the overall scattered intensity. However, outrunning radiation damage does not circumvate photoionization and it is therefore said that short pulses only reach a certain resolution [80]. So, it is a particular question, whether electron densities and here particular bonding configuration are obtainable by solely outrunning radiation damage. As radiation damage is unavoidable it can be mitigated in several ways. As the underlying processes are well understood, one way to mitigate for the radiation damage would be to computer model the effects, however, this can only be done for small particles. Another way to fundamentally increase resolution in single particle imaging is due to prior alignment of particles such that their orientation is know. While this has seen some success for small molecules [81], it is currently unknown, whether this works for larger molecules as the strong light fields, which are needed to align the molecules, may change their structure. Recent advances with phase-reconstruction algorithms made it possible to computationally determine the orientation of the particle at the time of imaging [82, 83] without prior knowledge if at least a few hundred images are provided. Thus, making molecule alignment a niche application. In this thesis, we shall discuss a method to reduce effects of damage is through artificial tampered layers. Artificial shells around a sample supply it with electrons and function as sacrificial layer that protects the sample [84]. For aerosol particles, this method has also only been investigated through ion spectroscopy [85, 86]. In the study shown in figure 2.18 a core-shell system of argon and xenon was constructed and, here, the xenon compares to the sample and the argon compares to the sacrificial layer around the particle (see figure). The heterogeneous cluster were irradiated with 93eV photons from *FLASH*[23] at which mostly xenon atoms are ionized. As described in the nanoplasma creation process (see section 2.5.1), the increasing ionized cluster creates a steep Coulomb potential trapping electrons. Trapped electrons are available for recombination with the ionized atoms.

---

[23] Short for **F**ree electron **LAS**er in **H**amburg. An extreme ultra violet (XUV) free electron laser in Hamburg, Germany.

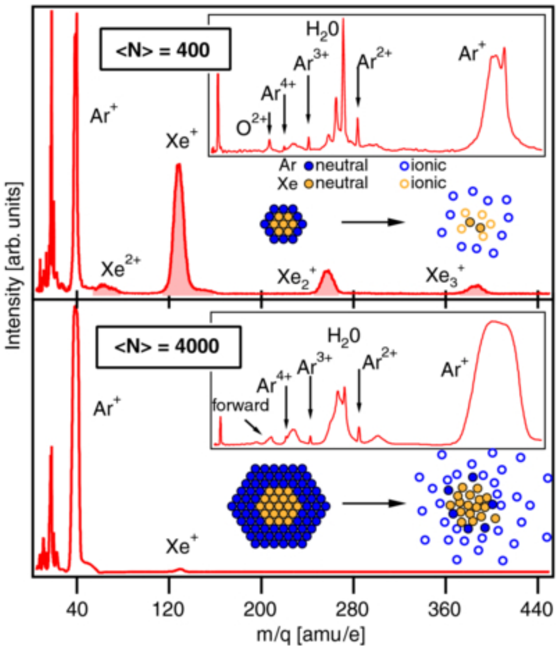

Figure 2.18: Time of flight (TOF) traces of argon and xenon core shell systems irradiated with 93eV X-ray pulses from FLASH. At this energy, mostly Xe is ionized and the ionized atoms create strong Coulomb potential that traps electrons towards the center of the cluster. The top panel shows smaller clusters with 400 particles, in which the trapping is inefficient, few electron-ion recombinations occur, thus Xe and Ar ions are detected in the TOF detector. The bottom panel shows large clusters with 4000 particles and thicker argon shell, here Xe-ions recombine in the center and the TOF shows mostly Ar ions as the neutral Xe remains undetected. at different sizes. From [85, 🅭🅯].

In the small core-shell system of Ar-Xe with 400 particles (figure 2.18 top-panel), the time of flight mass spectroscopy data shows Xe and Ar ions meaning that the charge recombination is suppressed and the cluster disintegrates upon irradiation. In the large Ar-Xe cluster system with 4000 particles (bottom-panel), mostly Ar ions are in the TOF data meaning the Xe ions in the center of the cluster recombine with the electrons that were attracted to the center by the steep Coulomb potential of the large cluster. The neutral Xe is not detected by the TOF detector. The Ar ions in the outer layers contributed electrons to the center of the cluster due to the attractive potential but were shed off the cluster. It is also evident that the argon atoms in the large cluster case release more kinetic energy than in the small cluster case, which is likely an effect that cools the intact cluster core.

3 Experimental Setup

3.1 The atomic, molecular and optcal physics instrument at LCLS

- Specifics to AMO
- For example focus studies and KBOs
- Use JSR and previous AMO articles

3.2 The LAMP end-station at AMO

- Specifics to the LAMP setup
- Use Journal of Synch. Radiation LAMP paper
- I think this can be a longer subsection since a lot of my work went into this.

3.3 The large area pn-CCD detectors

- Reuse our work on the LAMp-pnCCD paper
- I think this should be a longer chapter since a lot of my work has gone into this.

3.4 Time of flight mass-spectrometer

- fundamental aspects to the TOF detector
- I'm hoping on some specific drawings from Timur / LCLS and SIMION simulations from Timur here.

3.5 Sample delivery

4 Methods

4.1 The computing environment at LCLS

- Include basics around the PSANA interface
- For example how the date is converted, then stored and
- the analysis opportunities along the way - I think this will be a longer subsection since a lot of my work went into this and I'm regularly contacted about it. - Short introduction what we have to go through
- Reminder of detectors and analysis environment

4.1.1 PSANA - Python interaction with LCLS computing

4.2 pnCCD photon detectors

- Describe signal on the pnCCDs
- Calibrations and corrections - use LAMP paper
- single hits
- multiple hits

4.2.1 Signal analysis

- Present data from 1500eV photon energy on Xe backfilled chamber with the pnCCDs in spectroscopy mode to argue that the pedestal and offset corrections are enough to correct for fluoresence.
- Masked areas in image

4.3 Combining multiple pnCCD detectors

- Explain how I combined pnCCD detectors to perform reconstructions on it.
- Can reuse material from the LAMP pnCCD paper

4.4 Hitfinding

- Discuss the hitfinding.
- iTOF vs. pnCCD
- vs. Actual dynamics visible in diffraction images

4.5 Phase retrieval from a single diffraction pattern

- Short intro into phase retrieval

4.5.1 Solving the inverse problem

4.5.2 2D reconstructions and limitations

Hawk program

- Describe Filipe's program

Resolution enhancement through combination of rear and front pnCCD

- Showcase difference of rear pnCCD only vs. front + rear pnCCD vs. front + rear pnCCD 'cropped' for best results. Recycle work from LAMP pnCCD paper

4.5.3 1D reconstructions

- Describe my algorithm in 1D in detail

4.6 Summary of methods

- Comprehensive summary

5 Results and discussion

- Introduction of what we are looking for, reminder of hypothesis

5.1 Static data

5.2 Pristine xenon pump–probe data

- Presentation of Xe data

5.2.1 iToF traces with xenon as sample

- Xe iToF dynamics
- Slightly more of Xe higher charge-states present at longer delays.

5.2.2 Xenon diffraction images

- Present study of 1D condensed diffraction images.
- Work out similarities to Tais radiation damage

5.2.3 Reconstructions of xenon cluster single shot images

- Present Xe - cluster reconstructions
- Show 1D reconstructions and 'damage process'

5.2.4 pnCCD image pump – probe considerations

- Considerations of pump and probe pulse in one pnCCD image.

5.2.5 Time of flight data

5.3 Pristine helium cluster pump-probe data

- Presentation of He data

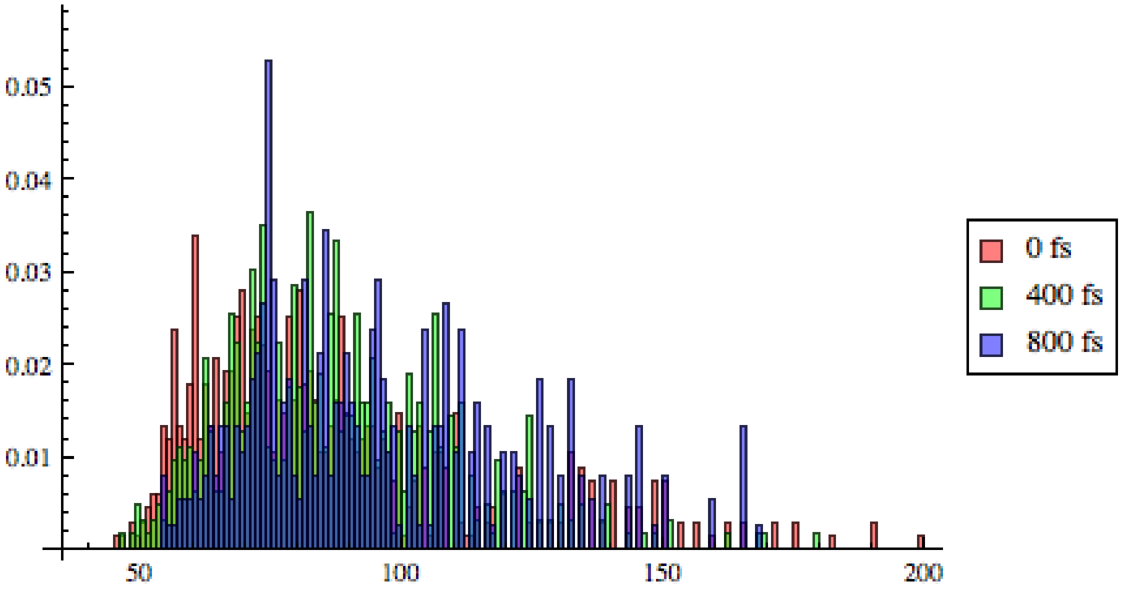

Figure 5.1: caption. MAKE IMAGE NICER

5.3.1 iToF data with helium as sample

- Subsection for iToF data, important to compare to HeXe data.

5.3.2 Diffraction images of helium cluster

- Work out radiation damage in 1D diffraction images.
- Introduce envelope to show the radiation damage effect - important to compare to HeXe data.
- Eventually subsection for reconstructions.

5.4 Helium-xenon core-shell systems and pump–probe data

-Presentation of HeXe data

5.4.1 Time-of-flight data of helium-xenon core-shell systems

- Show dynamics of XeHe data in tof trace.
- More hefty nanoplasma expansion in HeXe than in raw He.
- Complement with simulations from Phay.

5.4.2 Diffraction images of helium-xenon core shell systems

- Discuss diffraction images
- Show how scattering intensity drops from He signal but not from Xe signal.
- Eventually subsection for reconstructions.

5.4.3 Core-shell system considerations

5.5 Conclusion of the X-ray pump – X-ray probe study

- Conclusion where the results are compared to each other
- This experiment shows that heterogeneous clusters, as in tampered layers, do inhibit radiation damage of the sample target while the sacrificial layer undergoes a rapid nanoplasma transition.

6 Summary and outlook

6.1 Summary

Summary here

6.2 Outlook

Outlook here

7 Appendix

7.1 Python code on spherical integrations

7.2 Python code on combining detectors

8 Bibliography

[1] Sebastian Schorb. *Size-dependent ultrafast ionization dynamics of nanoscale samples in intense femtosecond x-ray free-electron laser pulses.* Thesis, Technische Universitat Berlin, 2012.

[2] C. Pellegrini, A. Marinelli, and S. Reiche. The physics of x-ray free-electron lasers. *Reviews of Modern Physics*, 88(1):1–55, 2016. ISSN 15390756. doi: 10.1103/RevModPhys.88.015006.

[3] Christoph Bostedt, Sébastien Boutet, David M. Fritz, Zhirong Huang, Hae Ja Lee, Henrik T. Lemke, Aymeric Robert, William F. Schlotter, Joshua J. Turner, and Garth J. Williams. Linac coherent light source: The first five years. *Rev. Mod. Phys.*, 88:015007, Mar 2016. doi: 10.1103/RevModPhys.88.015007. URL `http://link.aps.org/doi/10.1103/RevModPhys.88.015007`.

[4] D. M. Mills, J. R. Helliwell, Å Kvick, T. Ohta, I. A. Robinson, and A. Authier. Report of the working group on synchrotron radiation nomenclature - Brightness, spectral brightness or brilliance? *Journal of Synchrotron Radiation*, 12(3):385, 2005. ISSN 09090495. doi: 10.1107/S090904950500796X.

[5] Jens Als-Nielsen and Des McMorrow. *Elements of modern X-ray physics.* John Wiley & Sons, 2011.

[6] SLAC National Accelerator Laboratory. Lcls aerial overlay, 2009. URL `https://www.flickr.com/photos/slaclab/8577624017/`. Downloaded from SLAC's Flickr.

[7] Philip H. Bucksbaum, Ryan Coffee, and Nora Berrah. *Chapter 5 - The First Atomic and Molecular Experiments at the Linac Coherent Light Source X-Ray Free Electron Laser*, volume Volume 60, pages 239–289. Academic Press, 2011. ISBN 1049-250X. doi: http://dx.doi.org/10.1016/B978-0-12-385508-4.00005-X. URL `http://www.sciencedirect.com/science/article/pii/B978012385508400005X`.

[8] G J Williams. personal communication, 2016.

[9] Jeff Hecht. The history of the x-ray laser. *Optics and Photonics News*, 19(5):26–33, 2008.

[10] A.M. Kondratenko and E. L. Saldin. Generation of coherent radiation by a relativistic electron beam in an ondulator*. *Particle Accelerators*, 10:207–216, 1980. doi: 1003-0207.

[11] R. Bonifacio, C. Pellegrini, and L. M. Narducci. Collective instabilities and high-gain regime in a free electron laser. *Optics Communications*, 50(6):373–378, 1984. ISSN 00304018. doi: 10.1016/0030-4018(84)90105-6.

[12] Bastian Holst and Arpad Horvath. Undulator, Jul 2005. URL `https://commons.wikimedia.org/wiki/file:undulator.png`.

[13] G. Brown, K. Halbach, J. Harris, and H. Winick. Wiggler and undulator magnets — A review. *Nuclear Instruments and Methods in Physics Research*, 208(1-3):65–77, apr 1983. ISSN 01675087. doi: 10.1016/0167-5087(83)91105-5. URL `http://linkinghub.elsevier.com/retrieve/pii/0167508783911055`.

[14] Kwang-Je Kim. Angular distribution of undulator power for an arbitrary deflection parameter K. *Nuclear Instruments and Methods in Physics Research Section A: Accelerators, Spectrometers, Detectors and Associated Equipment*, 246(1-3):67–70, may 1986. ISSN 01689002. doi: 10.1016/0168-9002(86)90047-1. URL `http://linkinghub.elsevier.com/retrieve/pii/0168900286900471`.

[15] Zhirong Huang and Kwang-Je Kim. Review of x-ray free-electron laser theory. *Phys. Rev. ST Accel. Beams*, 10:034801, Mar 2007. doi: 10.1103/PhysRevSTAB.10.034801. URL `http://link.aps.org/doi/10.1103/PhysRevSTAB.10.034801`.

[16] Daniela Rupp. *Ionization and plasma dynamics of single large xenon clusters in superintense XUV pulses.* Thesis, Technische Universität Berlin, 2013.

[17] Daniela Rupp. *Ionization and plasma dynamics of single large xenon clusters in superintense XUV pulses.* Springer, 2016.

[18] M. Bucher, K. R. Ferguson, Gorkhover T., and Bostedt C. A transmissive single-shot soft x-ray spectrometer. Unpublished study on feasibility of a spectrometer that is based on photoemission., 2014.

[19] L. B. Fletcher, H. J. Lee, T. Döppner, E. Galtier, B. Nagler, P. Heimann, C. Fortmann, S. LePape, T. Ma, M. Millot, et al. Ultrabright x-ray laser scattering for

dynamic warm dense matter physics. *Nat. Photonics*, 2015. ISSN 1748-0221. doi: 10.1038/nphoton.2015.41.

[20] J. Amann, W. Berg, V. Blank, F. J. Decker, Y. Ding, P. Emma, Y. Feng, J. Frisch, D. Fritz, J. Hastings, et al. Demonstration of self-seeding in a hard-x-ray free-electron laser. *Nat. Photonics*, 6(10):693–698, 2012. ISSN 1749-4885. doi: 10.1038/NPHOTON.2012.180. URL `http://www.nature.com/nphoton/journal/v6/n10/pdf/nphoton.2012.180.pdf`.

[21] D. Ratner, R. Abela, J. Amann, C. Behrens, D. Bohler, G. Bouchard, C. Bostedt, M. Boyes, K. Chow, D. Cocco, F. J. Decker, Y. Ding, C. Eckman, P. Emma, D. Fairley, Y. Feng, C. Field, U. Flechsig, G. Gassner, J. Hastings, P. Heimann, Z. Huang, N. Kelez, J. Krzywinski, H. Loos, A. Lutman, A. Marinelli, G. Marcus, T. Maxwell, P. Montanez, S. Moeller, D. Morton, H. D. Nuhn, N. Rodes, W. Schlotter, S. Serkez, T. Stevens, J. Turner, D. Walz, J. Welch, and J. Wu. Experimental demonstration of a soft x-ray self-seeded free-electron laser. *Phys. Rev. Lett.*, 114:054801, Feb 2015. doi: 10.1103/PhysRevLett.114.054801. URL `http://link.aps.org/doi/10.1103/PhysRevLett.114.054801`.

[22] K. R. Ferguson, M. Bucher, T. Gorkhover, and Bostedt C. Absorption spectroscopy on co and CO_2 molecules. Unpublished study on CO and CO_2 molceules using an ion time of flight spectrometer that is proportional to the ion yield., 2014.

[23] Victor Kimberg, Alvaro Sanchez-Gonzalez, Laurent Mercadier, Clemens Weninger, Alberto Lutman, Daniel Ratner, Ryan N Coffee, Maximilian Bucher, Melanie Mucke, Marcus Agaker, Conny Sathe, Christoph Bostedt, Joseph Nordgren, Jan-Erik Rubensson, and Nina Rohringer. Stimulated x-ray raman scattering - a critical assessment of the building block of nonlinear x-ray spectroscopy. *Faraday Discuss.*, pages –, 2016. doi: 10.1039/C6FD00103C. URL `http://dx.doi.org/10.1039/C6FD00103C`.

[24] J. C. Castagna, B. Murphy, J. Bozek, and N. Berrah. X-ray split and delay system for soft x-rays at lcls. *J. Phys.: Conf. Ser.*, 425(15):152021, 2013. ISSN 1742-6596. doi: 10.1088/1742-6596/425/15/152021. URL `http://iopscience.iop.org/1742-6596/425/15/152021`.

[25] Brendan F. Murphy, Jean-Charles Castagna, John D. Bozek, and Nora Berrah. Mirror-based soft x-ray split-and-delay system for femtosecond pump-probe experiments at lcls. In *X-Ray Free-Electron Lasers: Beam Diagnostics, Beamline In-*

strumentation, and Applications, volume 8504, pages 850409–850409–7, 2012. doi: 10.1117/12.928538. URL `http://dx.doi.org/10.1117/12.928538`.

[26] A. A. Lutman, R. Coffee, Y. Ding, Z. Huang, J. Krzywinski, T. Maxwell, M. Messerschmidt, and H. D. Nuhn. Experimental demonstration of femtosecond two-color x-ray free-electron lasers. *Phys. Rev. Lett.*, 110(13):134801, 2013. ISSN 0031-9007.

[27] A Marinelli, D Ratner, AA Lutman, J Turner, J Welch, F-J Decker, H Loos, C Behrens, S Gilevich, AA Miahnahri, et al. High-intensity double-pulse x-ray free-electron laser. *Nature communications*, 6, 2015.

[28] A. Picón, C. S. Lehmann, C. Bostedt, A. Rudenko, A. Marinelli, T. Osipov, D. Rolles, N. Berrah, C. Bomme, M. Bucher, G. Doumy, B. Erk, K. R. Ferguson, T. Gorkhover, P. J. Ho, E. P. Kanter, B. Krässig, J Krzywinski, A A Lutman, A M March, D Moonshiram, D Ray, L Young, S T Pratt, and S. H. Southworth. Hetero-site-specific X-ray pump-probe spectroscopy for femtosecond intramolecular dynamics. *Nature Communications*, 7(May):11652, 2016. ISSN 2041-1723. doi: 10.1038/ncomms11652. URL `http://www.nature.com/doifinder/10.1038/ncomms11652`.

[29] Ken R. Ferguson, Maximilian Bucher, Tais Gorkhover, Sébastien Boutet, Hironobu Fukuzawa, Jason E. Koglin, Yoshiaki Kumagai, Alberto Lutman, Agostino Marinelli, Marc Messerschmidt, Kiyonobu Nagaya, Jim Turner, Kiyoshi Ueda, Garth J. Williams, Philip H. Bucksbaum, and Christoph Bostedt. Transient lattice contraction in the solid-to-plasma transition. *Science Advances*, 2(1), 2016. doi: 10.1126/sciadv.1500837. URL `http://advances.sciencemag.org/content/2/1/e1500837`.

[30] Chelsea E Liekhus-Schmaltz, Ian Tenney, Timur Osipov, Alvaro Sanchez-Gonzalez, Nora Berrah, Rebecca Boll, Cedric Bomme, Christoph Bostedt, John D Bozek, Sebastian Carron, Ryan Coffee, Julien Devin, Benjamin Erk, Ken R Ferguson, Robert W Field, Lutz Foucar, Leszek J Frasinski, James M Glownia, Markus Gühr, Andrei Kamalov, Jacek Krzywinski, Heng Li, Jonathan P Marangos, Todd J Martinez, Brian K McFarland, Shungo Miyabe, Brendan Murphy, Adi Natan, Daniel Rolles, Artem Rudenko, Marco Siano, Emma R Simpson, Limor Spector, Michele Swiggers, Daniel Walke, Song Wang, Thorsten Weber, Philip H Bucksbaum, and Vladimir S Petrovic. Ultrafast isomerization initiated by X-ray core ionization. *Nature communications*, 6:8199, 2015. ISSN 2041-1723. doi: 10.1038/ncomms9199. URL `http://www.ncbi.nlm.nih.gov/pubmed/26354002`.

F

[31] P. Emma, K. Bane, M. Cornacchia, Z. Huang, H. Schlarb, G. Stupakov, and D. Walz. Femtosecond and subfemtosecond x-ray pulses from a self-amplified spontaneous-emission–based free-electron laser. *Phys. Rev. Lett.*, 92(7):074801, 2004.

[32] H Haberland. *Clusters of atoms and Molecules I, vol. 52 of Springer Series in Chemical Physics*. Springer-Verlag, Berlin, 1994.

[33] W Miehle, O Kandler, T Leisner, and O Echt. Mass spectrometric evidence for icosahedral structure in large rare gas clusters: Ar, kr, xe. *The Journal of chemical physics*, 91(10):5940–5952, 1989.

[34] B W Vandewaal. Icosahedral, decahedral, fcc, and defect-fcc structural models for Ar-N clusters, n>=500 - how plausible are they? *J Chem Phys*, 98(6):4909–4919, 1993. ISSN 00219606. doi: 10.1063/1.464946.

[35] Nina V. Krainyukova. 'The crystal structure problem' in noble gas nanoclusters. *Thin Solid Films*, 515(4):1658–1663, 2006. ISSN 00406090. doi: 10.1016/j.tsf.2006.05.041.

[36] D. Lippmann, W. C. Schieve, and C. Canestaro. Clustering time dependence in molecular dynamics: A kinetic model. *The Journal of Chemical Physics*, 81(11):4969, 1984. ISSN 00219606. doi: 10.1063/1.447481. URL `http://link.aip.org/link/JCPSA6/v81/i11/p4969/s1{&}Agg=doi`.

[37] W.H. Zurek and W.C. Shieve. Multistep Clustering and Nucleation. *Journal of Physical Chemistry*, 84(12):1479–1482, 1980. ISSN 0022-3654. doi: 10.1021/j100449a010.

[38] J. M. Soler, N. García, O. Echt, K. Sattler, and E. Recknagel. Microcluster growth: Transition from successive monomer addition to coagulation. *Phys. Rev. Lett.*, 49:1857–1860, Dec 1982. doi: 10.1103/PhysRevLett.49.1857. URL `http://link.aps.org/doi/10.1103/PhysRevLett.49.1857`.

[39] David R. Miller. Free jet sources. In Giacinto Scoles, editor, *Atomic and Molecular Beam Methods*, chapter 2, pages 14–53. Oxford University Press, Inc., 1988.

[40] I. Yamada, J. Matsuo, N. Toyoda, and A. Kirkpatrick. Materials processing by gas cluster ion beams. *Materials Science and Engineering: R: Reports*, 34(6):231–295, 2001. ISSN 0927796X. doi: 10.1016/S0927-796X(01)00034-1. URL `http://www.sciencedirect.com/science/article/pii/S0927796X01000341`.

[41] J. Farges, M. F. de Feraudy, B. Raoult, and G. Torchet. Structure and temperature of rare gas clusters in a supersonic expansion. *Surface Science*, 106(1-3):95–100, 1981. ISSN 00396028. doi: 10.1016/0039-6028(81)90186-2.

[42] J Gspann. On the phase of metal clusters. In Frank Träger and Gisbert zu Putlitz, editors, *Metal Clusters*, pages 43–45, Berlin, Heidelberg, April 1986. Springer Berlin Heidelberg. ISBN 978-3-642-71571-6. URL `http://dx.doi.org/10.1007/978-3-642-71571-6{_}7`.

[43] Otto F. Hagena. Cluster Formation in Expanding Supersonic Jets: Effect of Pressure, Temperature, Nozzle Size, and Test Gas. *The Journal of Chemical Physics*, 56(5):1793, 1972. ISSN 00219606. doi: 10.1063/1.1677455. URL `http://scitation.aip.org/content/aip/journal/jcp/56/5/10.1063/1.1677455`.

[44] Otto F. Hagena. Nucleation and growth of clusters in expanding nozzle flows. *Surface Science*, 106(1-3):101–116, 1981. ISSN 00396028. doi: 10.1016/0039-6028(81)90187-4.

[45] Otto F. Hagena. Condensation in free jets: Comparison of rare gases and metals. *Zeitschrift für Physik D Atoms, Molecules and Clusters*, 4(3):291–299, 1987. ISSN 01787683. doi: 10.1007/BF01436638.

[46] Lawrence S Bartell. Diffraction studies of clusters generated in supersonic flow. *Chemical Reviews*, 86(3):491, 1986. ISSN 0009-2665. doi: 10.1021/cr00073a001.

[47] Daniela Rupp, Marcus Adolph, Leonie Fl??ckiger, Tais Gorkhover, Jan Philippe Müller, Maria Müller, Mario Sauppe, David Wolter, Sebastian Schorb, Rolf Treusch, Christoph Bostedt, and Thomas Möller. Generation and structure of extremely large clusters in pulsed jets. *Journal of Chemical Physics*, 141(4), 2014. ISSN 00219606. doi: 10.1063/1.4890323. URL `http://dx.doi.org/10.1063/1.4890323`.

[48] T. E. Gough, M. Mengel, P. a. Rowntree, and G. Scoles. Infrared spectroscopy at the surface of clusters: SF6 on Ar. *The Journal of Chemical Physics*, 83(10):4958, 1985. ISSN 00219606. doi: 10.1063/1.449757. URL `http://scitation.aip.org/content/aip/journal/jcp/83/10/10.1063/1.449757`.

[49] Luis F. Gomez, Evgeny Loginov, Russell Sliter, and Andrey F. Vilesov. Sizes of large He droplets. *Journal of Chemical Physics*, 135(15), 2011. ISSN 00219606. doi: 10.1063/1.3650235.

[50] Luis F. Gomez, Ken R. Ferguson, James P. Cryan, Camila Bacellar, Rico Mayro P. Tanyag, Curtis Jones, Sebastian Schorb, Denis Anielski, Ali Belkacem, Charles Bernando, et al. Shapes and vorticities of superfluid helium nanodroplets. *Science*, 345(6199):906–909, 2014.

[51] André Guinier and Gérard Fournet. *Small-angle scattering of X-rays.* J. Wiley & Sons, New York, 1955.

[52] J R Fienup. Phase retrieval algorithms: a comparison. *Applied Optics*, 21 (15):2758–2769, 1982. ISSN 0003-6935. doi: 10.1364/AO.21.002758. URL `http://www.opticsinfobase.org.ezproxy.lib.purdue.edu/viewmedia.cfm?uri=ao-21-15-2758{&}seq=0{&}html=true$\delimiter"026E30F$npapers3://publication/doi/10.1364/AO.21.002758`.

[53] J R Fienup. Reconstruction of an object from the modulus of its Fourier transform. *Optics letters*, 3(1):27–29, 1978. ISSN 0146-9592. doi: 10.1364/OL.3.000027.

[54] D Russell Luke. Relaxed averaged alternating reflections for diffraction imaging. *Inverse Problems*, 21(1):37, 2005. URL `http://stacks.iop.org/0266-5611/21/i=1/a=004`.

[55] David Attwood. *Soft x-rays and extreme ultraviolet radiation.* Cambridge university press, 2000. ISBN 0-521-65214-6.

[56] Atomic calculation of photoionization cross-sections and asymmetry parameters, August 2016. URL `https://vuo.elettra.eu/services/elements/WebElements.html`.

[57] JJ Yeh and I Lindau. Atomic subshell photoionization cross sections and asymmetry parameters: 1$\geq$ z $\geq$ 103. *Atomic data and nuclear data tables*, 32(1):1–155, 1985.

[58] J-J Yeh. *Atomic calculation of photoionization cross-sections and asymmetry parameters.* Gordon & Breach Science Publ.; AT&T Bell Laboratories, 1993.

[59] Robert D Cowan. *The theory of atomic structure and spectra.* University of California Press, 1981. URL `http://aphysics2.lanl.gov/tempweb/lanl/`.

[60] Wolfgang Demtröder. *Experimentalphysik 3: Atome, Moleküle und Festkörper.* Springer Verlag, 2005.

[61] Phay J. Ho. personal communication, August 2016.

[62] M. Bucher, K. R. Ferguson, Gorkhover T., and Bostedt C. The lamp endstation in the amo instrument at the linac coherent light source. Unpublished study on the LAMP endstation with focus on the pnCCD detectors., 2016.

[63] B. Rudek, S. K. Son, L. Foucar, S. W. Epp, B. Erk, R. Hartmann, M. Adolph, R. Andritschke, A. Aquila, N. Berrah, et al. Ultra-efficient ionization of heavy atoms by intense x-ray free-electron laser pulses. *Nat. Photonics*, 6(12):858–865, 2012. ISSN 1749-4885. doi: 10.1038/Nphoton.2012.261.

[64] M.O. Krause, F.A. Stevie, L.J. Lewis, T.A. Carlson, and W.E. Moddeman. Multiple excitation of neon by photon and electron impact. *Physics Letters A*, 31(2):81–82, jan 1970. ISSN 03759601. doi: 10.1016/0375-9601(70)91039-X. URL `http://linkinghub.elsevier.com/retrieve/pii/037596017091039X`.

[] D. Coster and R. De L. Kronig. New type of auger effect and its influence on the x-ray spectrum. *Physica*, 2(1-12):13–24, jan 1935. ISSN 00318914. doi: 10.1016/S0031-8914(35)90060-X. URL `http://linkinghub.elsevier.com/retrieve/pii/S003189143590060X`.

[65] Mathias Arbeiter and Thomas Fennel. Rare-gas clusters in intense vuv, xuv and soft x-ray pulses: signatures of the transition from nanoplasma-driven cluster expansion to coulomb explosion in ion and electron spectra. *New Journal of Physics*, 13(5): 053022, 2011. doi: http://dx.doi.org/10.1088/1367-2630/13/5/053022.

[66] C Bostedt, M Adolph, E Eremina, M Hoener, D Rupp, S Schorb, H Thomas, A R B de Castro, and T Möller. Clusters in intense FLASH pulses: ultrafast ionization dynamics and electron emission studied with spectroscopic and scattering techniques. *Journal of Physics B: Atomic, Molecular and Optical Physics*, 43:194011, 2010. ISSN 0953-4075. doi: 10.1088/0953-4075/43/19/194011.

[67] H Wabnitz, L Bittner, a R B de Castro, R Döhrmann, P Gürtler, T Laarmann, W Laasch, J Schulz, A Swiderski, K von Haeften, T Möller, B Faatz, A Fateev, J Feldhaus, C Gerth, U Hahn, E Saldin, E Schneidmiller, K Sytchev, K Tiedtke, R Treusch, and M Yurkov. Multiple ionization of atom clusters by intense soft X-rays from a free-electron laser. *Nature*, 420(6915):482–5, 2002. ISSN 0028-0836. doi: 10.1038/nature01197. URL `http://www.ncbi.nlm.nih.gov/pubmed/12466837`.

[68] T. Laarmann, A. R B De Castro, P. Gürtler, W. Laasch, J. Schulz, H. Wabnitz, and T. Möller. Interaction of Argon clusters with intense VUV-laser radiation: The role

of electronic structure in the energy-deposition process. *Physical Review Letters*, 92 (14):143401–1, 2004. ISSN 00319007. doi: 10.1103/PhysRevLett.92.143401.

[69] C. Bostedt, H. Thomas, M. Hoener, E. Eremina, T. Fennel, K. H. Meiwes-Broer, H. Wabnitz, M. Kuhlmann, E. Plönjes, K. Tiedtke, R. Treusch, J. Feldhaus, A. R B De Castro, and T. Möller. Multistep ionization of argon clusters in intense femtosecond extreme ultraviolet pulses. *Physical Review Letters*, 100(13):12–14, 2008. ISSN 00319007. doi: 10.1103/PhysRevLett.100.133401.

[70] T. Laarmann, M. Rusek, H. Wabnitz, J. Schulz, A. R B De Castro, P. Gürtler, W. Laasch, and T. Möller. Emission of thermally activated electrons from rare gas clusters irradiated with intense VUV light pulses from a free electron laser. *Physical Review Letters*, 95(6):3–6, 2005. ISSN 00319007. doi: 10.1103/PhysRevLett.95.063402.

[71] Christoph Bostedt, Heiko Thomas, Matthias Hoener, Thomas M??ller, Ulf Saalmann, Ionu?? Georgescu, Christian Gnodtke, and Jan Michael Rost. Fast electrons from multi-electron dynamics in xenon clusters induced by inner-shell ionization. *New Journal of Physics*, 12, 2010. ISSN 13672630. doi: 10.1088/1367-2630/12/8/083004.

[72] Mathias Arbeiter and Thomas Fennel. Ionization heating in rare-gas clusters under intense XUV laser pulses. *Physical Review A - Atomic, Molecular, and Optical Physics*, 82(1):1–7, 2010. ISSN 10502947. doi: 10.1103/PhysRevA.82.013201.

[73] M. Lezius, S. Dobosz, D. Normand, and M. Schmidt. Explosion Dynamics of Rare Gas Clusters in Strong Laser Fields. *Physical Review Letters*, 80(2):261–264, 1998. ISSN 0031-9007. doi: 10.1103/PhysRevLett.80.261.

[74] Tais Gorkhover, Sebastian Schorb, Ryan Coffee, Marcus Adolph, Lutz Foucar, Daniela Rupp, Andrew Aquila, John D. Bozek, Sascha W. Epp, Benjamin Erk, Lars Gumprecht, Lotte Holmegaard, Andreas Hartmann, Robert Hartmann, Günter Hauser, Peter Holl, Andre Hömke, Per Johnsson, Nils Kimmel, Kai-Uwe Kühnel, Marc Messerschmidt, Christian Reich, Arnaud Rouzée, Benedikt Rudek, Carlo Schmidt, Joachim Schulz, Heike Soltau, Stephan Stern, Georg Weidenspointner, Bill White, Jochen Küpper, Lothar Strüder, Ilme Schlichting, Joachim Ullrich, Daniel Rolles, Artem Rudenko, Thomas Möller, and Christoph Bostedt. Femtosecond and nanometre visualization of structural dynamics in superheated nanoparticles. *Na-*

ture Photonics, 10(2):93–97, 2016. ISSN 1749-4885. doi: 10.1038/nphoton.2015.264. URL `http://www.nature.com/doifinder/10.1038/nphoton.2015.264`.

[75] R. Neutze, R. Wouts, D. van der Spoel, E. Weckert, and J. Hajdu. Potential for biomolecular imaging with femtosecond x-ray pulses. *Nature*, 406(6797):752–757, 2000. ISSN 0028-0836. doi: 10.1038/35021099.

[76] C. Bostedt, E. Eremina, D. Rupp, M. Adolph, H. Thomas, M. Hoener, A. R. de Castro, J. Tiggesbaumker, K. H. Meiwes-Broer, T. Laarmann, et al. Ultrafast x-ray scattering of xenon nanoparticles: imaging transient states of matter. *Phys. Rev. Lett.*, 108(9):093401, 2012. ISSN 1079-7114. doi: 10.1103/PhysRevLett.108.093401. URL `http://journals.aps.org/prl/abstract/10.1103/PhysRevLett.108.093401`.

[77] T. Gorkhover, M. Adolph, D. Rupp, S. Schorb, S. W. Epp, B. Erk, L. Foucar, R. Hartmann, N. Kimmel, K. U. Kuhnel, et al. Nanoplasma dynamics of single large xenon clusters irradiated with superintense x-ray pulses from the linac coherent light source free-electron laser. *Phys. Rev. Lett.*, 108(24):245005, 2012. ISSN 1079-7114.

[78] Stefan P. Hau-Riege and Henry N. Chapman. Modeling of the damage dynamics of nanospheres exposed to x-ray free-electron-laser radiation. *Physical Review E - Statistical, Nonlinear, and Soft Matter Physics*, 77(4):1–4, 2008. ISSN 15393755. doi: 10.1103/PhysRevE.77.041902.

[79] Christian Peltz, Charles Varin, Thomas Brabec, and Thomas Fennel. Time-resolved x-ray imaging of anisotropic nanoplasma expansion. *Physical Review Letters*, 113 (3):1–6, 2014. ISSN 10797114. doi: 10.1103/PhysRevLett.113.133401.

[80] A. Aquila, A. Barty, C. Bostedt, S. Boutet, G. Carini, D. dePonte, P. Drell, S. Doniach, K. H. Downing, T. Earnest, et al. The linac coherent light source single particle imaging road map. *Structural Dynamics*, 2(4):041701, 2015. doi: http://dx.doi.org/10.1063/1.4918726.

[81] Jochen Küpper, Stephan Stern, Lotte Holmegaard, Frank Filsinger, Arnaud Rouzée, Artem Rudenko, Per Johnsson, Andrew V. Martin, Marcus Adolph, Andrew Aquila, et al. X-ray diffraction from isolated and strongly aligned gas-phase molecules with a free-electron laser. *Phys. Rev. Lett.*, 112(8):083002, 2014. URL `http://link.aps.org/doi/10.1103/PhysRevLett.112.083002`. PRL.

[82] Ne Te Duane Loh and Veit Elser. Reconstruction algorithm for single-particle diffraction imaging experiments. *Physical Review E - Statistical, Nonlinear, and Soft Matter Physics*, 80(2):1–20, 2009. ISSN 15393755. doi: 10.1103/PhysRevE.80.026705.

[83] Tomas Ekeberg, Martin Svenda, Chantal Abergel, Filipe R.N.C. Maia, Virginie Seltzer, Jean-Michel Claverie, Max Hantke, Olof Jonsson, Carl Nettelblad, Gijs van der Schot, et al. Three-dimensional reconstruction of the giant mimivirus particle with an x-ray free-electron laser. *Phys. Rev. Lett.*, 114:098102, Mar 2015. doi: 10.1103/PhysRevLett.114.098102.

[84] Stefan P. Hau-Riege, Sébastien Boutet, Anton Barty, Saša Bajt, Michael J. Bogan, Matthias Frank, Jakob Andreasson, Bianca Iwan, M. Marvin Seibert, Janos Hajdu, Anne Sakdinawat, Joachim Schulz, Rolf Treusch, and Henry N. Chapman. Sacrificial tamper slows down sample explosion in FLASH dffraction eperiments. *Physical Review Letters*, 104(February):1–4, 2010. ISSN 00319007. doi: 10.1103/PhysRevLett.104.064801.

[85] Matthias Hoener, Christoph Bostedt, H. Thomas, L. Landt, E. Eremina, H. Wabnitz, T. Laarmann, R. Treusch, A. R. B. De Castro, and Thomas Möller. Charge recombination in soft x-ray laser produced nanoplasmas. *Journal of Physics B: Atomic, Molecular and Optical Physics*, 41(18):181001, 2008. ISSN 0953-4075. doi: 10.1088/0953-4075/41/18/181001. URL `http://stacks.iop.org/0953-4075/41/i=18/a=181001?key=crossref.8294ba41a32aa89b0a6ec0f8b550687f$\delimiter"026E30F$nhttp://iopscience.iop.org/0953-4075/41/18/181001`.

[86] Michael Ziemkewitz, Camila Bacellar, Adam Chatterley, Maximilian Bucher, Kenneth Ferguson, Taisa Gorkhover, Maria Mueller, Daniela Rupp, Jones Curtis, Rico Mayro P. Tanyag, Charles Bernando, Luis Gomez, Justing Kwok, Sebastian Carron, James Cryan, Jacek Krzywinski, Alberto Lutmann, Agostino Marinelli, Timothy Maxwell, Jim Turner, Franz-Josef Decker, Daniel M. Neumark, Thomas Möller, Andrey Vilesov, Christoph Bostedt, and Oliver Gessner. Controlling explosion dynamics in mixed solid/superfluid clusters with x-ray double pulses. in preparation, 2017.

9 Index

amplitude
  complex, 28

Bragg’s law, 42
brilliance, *see also* spectral brightness

cluster size, 22
Coulomb potential, 39

dispersion correction
  complex, 32
dopant, 25

electron density
  expanding, 42
emittance, 10

Free electron LASer in Hamburg
  FLASH, 44, 45

Hagena, *see* scaling law
  scaling parameter, 22

ionization
  energy, 33
  inner, 39
  multistep, 39, 44

LCLS, *see also* Linac Coherent Light Source, 44
Linac Coherent Light Source, 6

microbunching, 10

nanoplasma
  transition, 39

photoionization, 33
pulse energy, 44

radiation damage, 44
refractive index, 31
  complex, 42

scaling law, 22
self-seeding, 10
  soft x-ray, 13
spectral brightness, 5

time of flight
  mass spectroscopy, 46

undulator, 8

10 Acknowledgment

This has to be written.

Q